

## VU Research Portal

### **A two-million-year-long hydroclimatic context for hominin evolution in southeastern Africa**

Caley, Thibaut; Extier, Thomas; Collins, James A.; Schefuß, Enno; Dupont, Lydie; Malaizé, Bruno; Rossignol, Linda; Souron, Antoine; McClymont, Erin L.; Jimenez-Espejo, Francisco J.; García-Comas, Carmen; Eynaud, Frédérique; Martinez, Philippe; Roche, Didier M.; Jorry, Stephan J.; Charlier, Karine; Wary, Mélanie; Gourves, Pierre Yves; Billy, Isabelle; Giraudeau, Jacques

***published in***

Nature

2018

***DOI (link to publisher)***

[10.1038/s41586-018-0309-6](https://doi.org/10.1038/s41586-018-0309-6)

***document version***

Publisher's PDF, also known as Version of record

***document license***

Article 25fa Dutch Copyright Act

[Link to publication in VU Research Portal](#)

***citation for published version (APA)***

Caley, T., Extier, T., Collins, J. A., Schefuß, E., Dupont, L., Malaizé, B., Rossignol, L., Souron, A., McClymont, E. L., Jimenez-Espejo, F. J., García-Comas, C., Eynaud, F., Martinez, P., Roche, D. M., Jorry, S. J., Charlier, K., Wary, M., Gourves, P. Y., Billy, I., & Giraudeau, J. (2018). A two-million-year-long hydroclimatic context for hominin evolution in southeastern Africa. *Nature*, 560(7716), 76-79. <https://doi.org/10.1038/s41586-018-0309-6>

**General rights**

Copyright and moral rights for the publications made accessible in the public portal are retained by the authors and/or other copyright owners and it is a condition of accessing publications that users recognise and abide by the legal requirements associated with these rights.

- Users may download and print one copy of any publication from the public portal for the purpose of private study or research.
- You may not further distribute the material or use it for any profit-making activity or commercial gain
- You may freely distribute the URL identifying the publication in the public portal ?

**Take down policy**

If you believe that this document breaches copyright please contact us providing details, and we will remove access to the work immediately and investigate your claim.

**E-mail address:**

[vuresearchportal.ub@vu.nl](mailto:vuresearchportal.ub@vu.nl)

# A two-million-year-long hydroclimatic context for hominin evolution in southeastern Africa

Thibaut Caley<sup>1\*</sup>, Thomas Extier<sup>1,2</sup>, James A. Collins<sup>3,4</sup>, Enno Schefuß<sup>5</sup>, Lydie Dupont<sup>5</sup>, Bruno Malaizé<sup>4</sup>, Linda Rossignol<sup>1</sup>, Antoine Souron<sup>6</sup>, Erin L. McClymont<sup>7</sup>, Francisco J. Jimenez-Espejo<sup>8</sup>, Carmen García-Comas<sup>9,10</sup>, Frédérique Eynaud<sup>1</sup>, Philippe Martinez<sup>1</sup>, Didier M. Roche<sup>2,11</sup>, Stephan J. Jorry<sup>12</sup>, Karine Charlier<sup>1</sup>, Mélanie Wary<sup>1</sup>, Pierre-Yves Gourves<sup>1</sup>, Isabelle Billy<sup>1</sup> & Jacques Giraudeau<sup>1</sup>

The past two million years of eastern African climate variability is currently poorly constrained, despite interest in understanding its assumed role in early human evolution<sup>1–4</sup>. Rare palaeoclimate records from northeastern Africa suggest progressively drier conditions<sup>2,5</sup> or a stable hydroclimate<sup>6</sup>. By contrast, records from Lake Malawi in tropical southeastern Africa reveal a trend of a progressively wetter climate over the past 1.3 million years<sup>7,8</sup>. The climatic forcings that controlled these past hydrological changes are also a matter of debate. Some studies suggest a dominant local insolation forcing on hydrological changes<sup>9–11</sup>, whereas others infer a potential influence of sea surface temperature changes in the Indian Ocean<sup>8,12,13</sup>. Here we show that the hydroclimate in southeastern Africa (20–25° S) is controlled by interplay between low-latitude insolation forcing (precession and eccentricity) and changes in ice volume at high latitudes. Our results are based on a multiple-proxy reconstruction of hydrological changes in the Limpopo River catchment, combined with a reconstruction of sea surface temperature in the southwestern Indian Ocean for the past 2.14 million years. We find a long-term aridification in the Limpopo catchment between around 1 and 0.6 million years ago, opposite to the hydroclimatic evolution suggested by records from Lake Malawi. Our results, together with evidence of wetting at Lake Malawi, imply that the rainbelt contracted toward the Equator in response to increased ice volume at high latitudes. By reducing the extent of woodland or wetlands in terrestrial ecosystems, the observed changes in the hydroclimate of southeastern Africa—both in terms of its long-term state and marked precessional variability—could have had a role in the evolution of early hominins, particularly in the extinction of *Paranthropus robustus*.

Subtropical southeastern Africa is a region of critical interest because it contains hominin fossils that enable a comparison between continental indicators of hominin evolution and nearby marine records of past climate changes. Different modes of climate change have previously been proposed as major factors that influenced hominin speciation, adaptation or extinction. Some authors stress the effect of long-term trends towards aridity on hominin evolution<sup>1,2</sup> whereas others suggest a crucial role of short periods of extreme climatic variability in driving hominin evolution<sup>3,4</sup>.

*P. robustus* fossils have been found only in southeastern Africa and exclusively in the Limpopo River catchment, at the sites of Cooper's Cave D, Drimolen, Swartkrans, Sterkfontein, Kromdraai B and Gondolin (Fig. 1) which date from at least about 2 million years ago (Ma) to 0.9 Ma (Extended Data Table 1). It is currently unclear whether climate stress could have had a role in the extinction of this species.

To investigate the hydroclimatic context of the environment in which *P. robustus* lived, we reconstructed changes in the Quaternary hydrological cycle in subtropical southeastern Africa (20–25° S) to determine the drivers of variability and to identify the long-term climate evolution of this region. We used marine sediment core MD96-2048 (26° 10' 482" S, 34° 01' 148" E, 660-m water depth) from offshore of the Limpopo River mouth (Fig. 1). The chronology of MD96-2048 is established by tuning the  $\delta^{18}\text{O}$  benthic foraminifera signal to the reference LR04 stack (Fig. 2, Methods), which confirms that the core covers the past 2.14 million years (Myr). We present a multiple-proxy record of hydrological changes in the Limpopo catchment together with a sea surface temperature (SST) record of the southwestern Indian Ocean (Fig. 2).

Modern precipitation in the Limpopo catchment is dominated by austral summer rainfall associated with the extension of the Intertropical Convergence Zone (ITCZ) southwards to 15–20° S (Fig. 1). Changes in the hydrological cycle in the catchment are imprinted on discharge from the Limpopo River. We observe large changes in sedimentary elemental ratios of terrestrial iron to marine calcium, which indicate changes in terrestrial discharge by the Limpopo River at orbital and longer timescales (Fig. 2, Extended Data Fig. 1). Maxima in  $\ln(\text{Fe}/\text{Ca})$  ratios are associated with a more-depleted stable hydrogen isotope composition of plant waxes ( $\delta\text{D}_{\text{wax}}$ ) (Fig. 2), which reflects the isotopic composition of precipitation and is indicative of a higher amount of regional rainfall<sup>10,12,14</sup> (Extended Data Fig. 2, Methods). Maxima in  $\ln(\text{Fe}/\text{Ca})$  ratios are also associated with maxima in concentrations of branched glycerol dialkyl glycerol tetraethers (brGDGT), which are commonly found in soils and attributed to Limpopo River runoff<sup>15</sup>, and more enriched plant-wax  $\delta^{13}\text{C}$ . A previous study of the past 0.8 Myr of core MD96-2048 interpreted shifts towards more-depleted  $\delta^{13}\text{C}_{\text{wax}}$  as potentially reflecting more-humid conditions<sup>16</sup>. However,  $\delta^{13}\text{C}_{\text{wax}}$  is a proxy for the contribution of waxes from  $\text{C}_3$  versus  $\text{C}_4$  plants to the sediments, which can be influenced by many other factors than aridity and humidity. We attribute the enriched plant  $\delta^{13}\text{C}_{\text{wax}}$  at times of depleted  $\delta\text{D}_{\text{wax}}$  values, and increased  $\ln(\text{Fe}/\text{Ca})$  and concentrations of brGDGT, to stronger transport of  $\text{C}_4$  plant material from the upper Limpopo catchment, in addition to the extension of riverine swamps and floodplains that contain abundant  $\text{C}_4$  sedges (Fig. 2, Extended Data Figs. 3, 4).

The  $\ln(\text{Fe}/\text{Ca})$  ratio has the highest temporal resolution—300 years on average—of the proxies that we used. Statistical analyses indicate significant 19- and 23-thousand-year (kyr) cycles (precession) and 100-kyr and 400-kyr cycles (eccentricity) but no significant 41-kyr cycle (obliquity) (Extended Data Fig. 5). The dominance of eccentricity and

<sup>1</sup>EPOC, UMR 5805, CNRS, University of Bordeaux, Pessac, France. <sup>2</sup>Laboratoire des Sciences du Climat et de l'Environnement, LSCE/IPSL, CEA-CNRS-UVSQ, Université Paris-Saclay, Gif-sur-Yvette, France. <sup>3</sup>GFZ – German Research Center for Geosciences, Section 5.1 Geomorphology, Organic Surface Geochemistry Laboratory, Potsdam, Germany. <sup>4</sup>Alfred Wegener Institute Helmholtz Centre for Polar and Marine Research, Bremerhaven, Germany. <sup>5</sup>MARUM – Center for Marine Environmental Sciences, University of Bremen, Bremen, Germany. <sup>6</sup>PACEA, UMR 5199, CNRS, University of Bordeaux, Pessac, France. <sup>7</sup>Department of Geography, Durham University, Durham, UK. <sup>8</sup>Department of Biogeochemistry (JAMSTEC), Yokosuka, Japan. <sup>9</sup>Research and Development Center for Global Change, (JAMSTEC), Yokohama, Japan. <sup>10</sup>Ecology Group, University of Vic – Central University of Catalonia, Barcelona, Spain. <sup>11</sup>Vrije Universiteit Amsterdam, Faculty of Science, Cluster Earth and Climate, Amsterdam, The Netherlands. <sup>12</sup>Unité Géosciences Marines, Institut Français de Recherche pour l'Exploitation de la Mer (IFREMER), Plouzané, France.

\*e-mail: thibaut.caley@u-bordeaux.fr

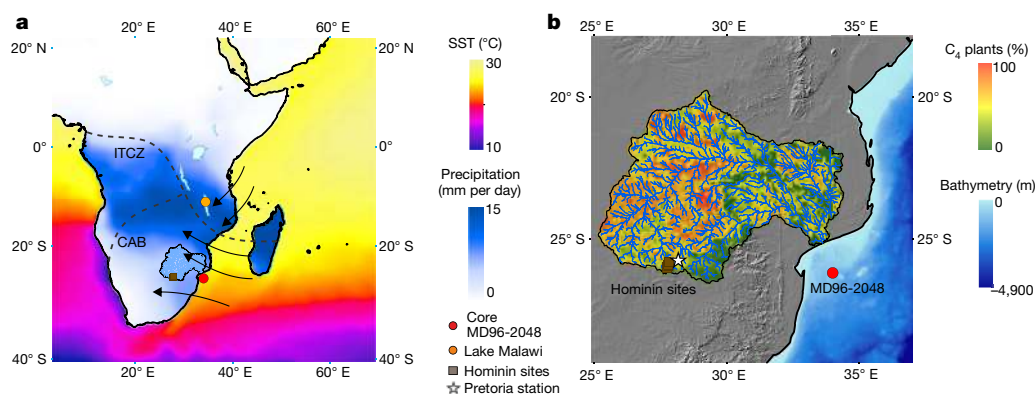


**Fig. 1 | Modern climatology over southern Africa and vegetation types in the Limpopo catchment.** **a**, Averaged precipitation rates for January<sup>28</sup> and annual SST over the Indian Ocean<sup>29</sup>. Black arrows represent the atmospheric circulation over southern Africa during austral summer. The ITCZ and the Congo air boundary (CAB) are indicated. **b**, Modelled relative C<sub>4</sub> plant abundance in the Limpopo catchment<sup>30</sup> with indications of topography (from SRTM, Shuttle Radar Topography Mission; <https://www2.jpl.nasa.gov/srtm/>) and bathymetry (from GEBCO, General Bathymetric Chart of the Oceans; <https://www.gebco.net>). Location of core MD96-2048, the Lake Malawi records, the main sites of hominin finds for *P. robustus* (sites of Cooper's Cave D, Drimolen, Swartkrans, Sterkfontein, Kromdraai B and Gondolin) and *A. sediba* (Malapa) (Extended Data Table 1) and the Pretoria Global Network of Isotopes in Precipitation station are indicated.

precession cycles indicates a strong influence of low-latitude insolation on hydrological changes in the Limpopo catchment. Rainfall and precession maxima are in phase (that is, maxima of local insolation in the Southern Hemisphere) (Extended Data Figs. 3, 5).

Modern-day rainfall in the subtropical Limpopo region depends mainly on easterly waves and low-pressure cells that largely control summer rainfall (November to March, 72% of the rainfall in Pretoria; Extended Data Fig. 2), and on tropical–extratropical cloud bands and associated thunderstorms<sup>17</sup>. Convective rains are usually associated with the ITCZ and warm, humid easterly winds<sup>17</sup>. Numerical model experiments suggest southern summer insolation forcing exerts a strong and positive effect on monsoon rainfall<sup>11,18</sup>. During precession maxima, higher levels of Southern Hemisphere summer insolation cause higher temperatures and lower surface pressure over the Southern Hemisphere, in particular over land<sup>11</sup>. The contrast between land and ocean temperatures results in stronger easterly moisture inflow into southeastern Africa. Increased rainfall results from increased convection over, and increased humidity transport into, southeastern Africa<sup>11</sup>. Because eccentricity modulates precession amplitudes, the increased summer insolation associated with eccentricity increases the variability in rainfall and fluvial discharge in the Limpopo catchment (Fig. 3).

In addition to this, it is thought that SST anomalies in the Indian Ocean have an influence on summer rainfall in the region<sup>19</sup>. To explore the potential relationship between hydrological cycle changes and oceanic conditions, we reconstructed SSTs for the southwestern Indian Ocean using two different methods (Extended Data Fig. 6, Methods). There is a significant correlation between SST and orbital parameters at the 100-kyr cycle (glacial–interglacial periodicity) and the 41-kyr cycle (obliquity) (Extended Data Fig. 5). The results confirm a previous study that revealed the absence of significant precessional variability in the SST record over the past 0.8 Myr<sup>15</sup>. This suggests that orbital-scale precipitation changes in southeastern Africa are more closely related to the contrast between land and ocean temperatures than to SST changes.

Superimposed on the orbital-scale changes, our record displays a long-term trend towards more arid conditions in southeastern Africa between about 1 and 0.6 Ma (Figs. 2, 3b, c). This period corresponds to the mid-Pleistocene transition (MPT), which is marked by ice-sheet expansion and global SST decrease<sup>20</sup> (Fig. 2). In terms of hydrological changes, the record from Lake Malawi that covers the past 1.3 Myr has previously been interpreted<sup>7,8</sup> to show changes that are opposite to those that we observe for the Limpopo catchment. At Lake Malawi, the climate changed from a predominantly arid environment between 1.3 and about 1 Ma to generally wetter conditions after about 1 Ma<sup>7,8</sup>. This opposing pattern in hydrological changes between the Limpopo

catchment and Lake Malawi suggests a gradual contraction of tropical rainfall from the Limpopo catchment towards lower latitudes in response to the ice sheet expansion during the MPT. This rainfall shift could be related to increased Antarctic ice volume during the MPT<sup>21,22</sup>.

The long-term trend towards wetter conditions at Lake Malawi has been explained by a progressively less-positive Indian Ocean Dipole since approximately 1 Ma. The Indian Ocean Dipole can enhance or reduce the precessional variability in the low-latitude hydroclimate by modifying the Walker circulation over the Indian Ocean, with a diverse response in eastern Africa<sup>23</sup>. A progressively less-positive Indian Ocean Dipole would have generated wetter conditions in southern Africa and increased the precession signal. Although the precessional signal increased over time in the Limpopo record, the observed progressive increase in aridity is contrary to what would be expected from Indian Ocean Dipole forcing alone (Fig. 3).

On the basis of our new records and comparisons with published records for Lake Malawi, we propose that low-latitude insolation forcing (precession and eccentricity) and changes in ice volume at high latitudes were the main drivers of the southeastern African hydroclimate over the past 2 Myr and that SST forcing had a secondary role. Our results also highlight a large regional variability in the southeastern African hydroclimate.

Changes in the hydrological cycle in southeastern Africa were probably one of multiple factors that influenced the dispersal and evolution of human relatives<sup>2,4</sup>. The more-humid conditions observed between about 2 Ma and 1.75 Ma, associated with a maximum in eccentricity forcing, correspond to several occurrences of *P. robustus* (Fig. 3, Extended Data Table 1). *P. robustus* is a species that was tolerant of environmental variability (eurytopic), but multiple lines of evidence suggest that from its earliest to its last occurrence this species preferred the wooded or humid components—dominated by C<sub>3</sub> plants—of environments that were otherwise dominated by C<sub>4</sub>, dry-adapted plants. This preference for habitats dominated by C<sub>3</sub> plants is well-corroborated by the data from palaeoecological studies of other contemporaneous animals that indicate that large quantities of C<sub>4</sub> vegetation were available, but that a more-wooded component and water sources were also present<sup>24</sup> (Fig. 3f, Extended Data Table 2, Methods). This more-humid period between about 2 Ma and 1.75 Ma is also characterized by the presence of *Australopithecus sediba* in the Limpopo catchment (so far known only from the Malapa site)<sup>25</sup>. Multiple lines of evidence suggest *A. sediba* also lived in a wooded or humid habitat and had a diet dominated by C<sub>3</sub> plants, within an otherwise rather-open environment dominated by C<sub>4</sub> plants<sup>25</sup>.

Our data raise the possibility that increasing long-term aridity associated with multi-millennial-scale changes after 1 Ma, driven by the

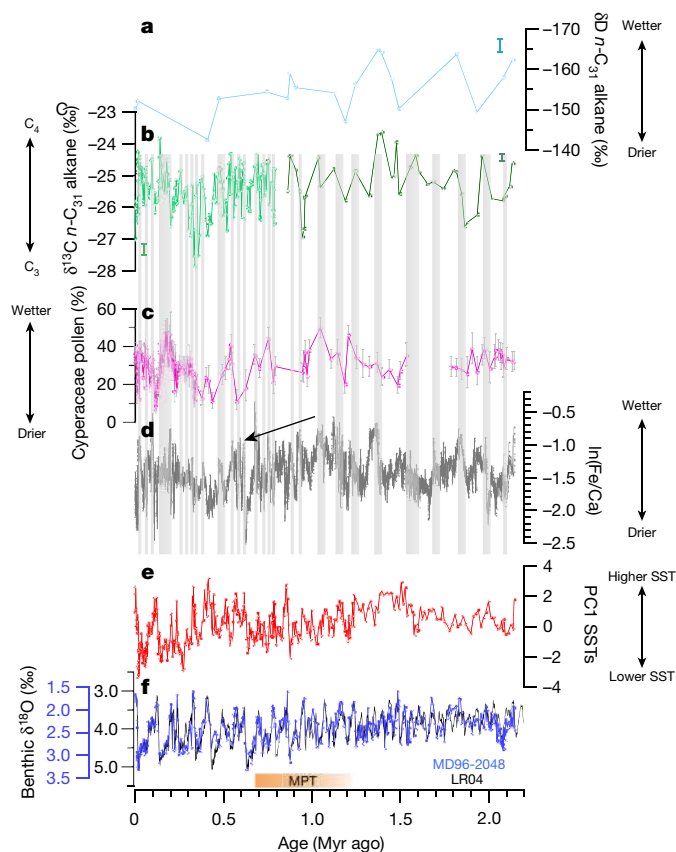


**Fig. 2 | Hydrological changes in the Limpopo catchment compared to SSTs of the southwestern Indian Ocean over the past 2.14 Myr.**

**a**,  $\delta D$  of the  $n\text{-C}_{31}$  alkane of plant waxes. Mean analytical uncertainty of 3‰ is indicated ( $n = 8$ ). **b**,  $\delta^{13}C$  of the  $n\text{-C}_{31}$  alkane of plant waxes. Data from a previous study<sup>16</sup> are shown in light green, and data from this study are shown in dark green. Mean analytical uncertainties of 0.2‰ ( $n = 15$ ) and average reproducibility of 0.4‰<sup>16</sup> are indicated. **c**, Pollen percentages of Cyperaceae (data from the past 342 kyr from a previous study<sup>13</sup>). Error bars represent 95% confidence intervals. **d**,  $\ln(\text{Fe}/\text{Ca})$  X-ray fluorescence (XRF) ratios. Arrow indicates the long-term trend discussed in the text. Grey frames represent events of hydrological cycle intensification. **e**, Principal component of the SST records (Methods). **f**,  $\delta^{18}O$  of benthic foraminifera compared to the reference LR04 curve (data from the past 790 kyr from a previously study<sup>15</sup>) (Methods). The MPT is indicated.

MPT (Fig. 3b–d), could have diminished the wooded and/or humid component of the habitat preferred by *P. robustus*. This is consistent with a trend towards more open and drier landscapes at Swartkrans (Fig. 3f, Extended Data Table 2, Methods).

It has previously been proposed that extinctions of large mammals are caused mainly by abiotic environmental changes<sup>26</sup>. We propose as a speculative, but plausible, scenario that the geographic ranges of species that preferred wooded and humid habitats—including *P. robustus*—would have contracted and expanded according to precessional (approximately 21-kyr) dry and wet cycles. During the multi-millennial dry periods, population ranges of these species would have contracted and often become fragmented. These isolated populations would have been especially prone to local extinction through lack of sufficient suitable food, water and shelter, and related increased competition and predation. During multi-millennial wet periods associated with precessional maxima, preferred woodland and humid habitats would have expanded again. The surviving populations would have expanded into their previously occupied range, replacing locally extinct populations. The long-term trend toward increased aridity implies that the dry periods became more and more pronounced between 1 and 0.6 Ma (Fig. 3b, d), increasing

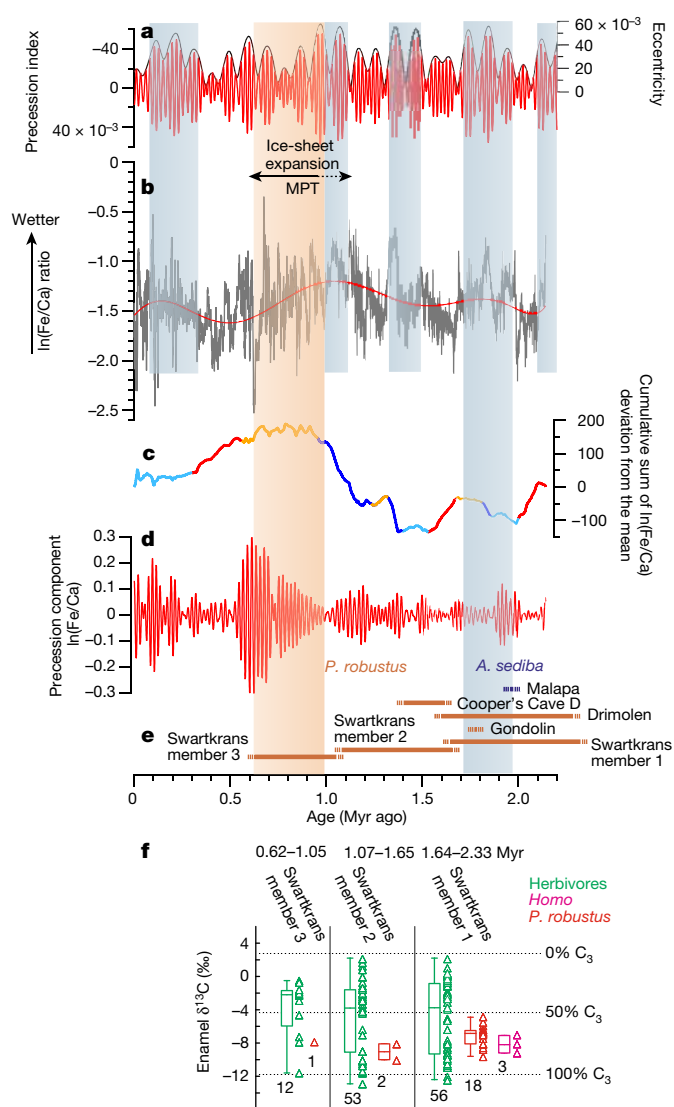


**Fig. 3 | Forcings on the hydrological cycle changes in the Limpopo catchment and relationship with hominin evolution over the past 2.14 Myr.**

**a**, Eccentricity and precession index<sup>31</sup>. **b**,  $\ln(\text{Fe}/\text{Ca})$  XRF ratios as a proxy for hydrological changes in the Limpopo catchment. Red curve denotes a polynomial fit (9th degree). The MPT and associated ice-sheet expansion is indicated (orange shading)<sup>20,21</sup>. Grey shading indicates wetter conditions in the Limpopo catchment, associated with higher eccentricity. **c**, Cumulative sum of  $\ln(\text{Fe}/\text{Ca})$  showing deviation from the mean as indicator of hydrological variability in the Limpopo catchment (Methods) (red curves correspond to dry periods, yellow curves to drying periods, dark blue curves to wet periods and light blue curves to humidification periods). **d**, Precession component of the  $\ln(\text{Fe}/\text{Ca})$  ratios obtained by Gaussian filtering. **e**, Estimated ages for the main sites that yielded remains of the hominins *P. robustus* (Cooper's Cave D, Drimolen, Swartkrans and Gondolin) and *A. sediba* (Malapa) (Extended Data Table 1). **f**, Enamel  $\delta^{13}C$  (‰ Vienna Pee Dee Belemnite) of hominins and contemporaneous herbivores at Swartkrans (Extended Data Table 2). Triangles indicate raw data points. The box plots correspond to the median (horizontal line), the interquartile range (box) and the full range of data (vertical whiskers). Sample sizes are indicated by numbers below the plots. Dashed lines highlight the thresholds used to estimate the percentage of  $C_3$  plants-derived foods in the diets.

the likelihood for more numerous extinctions of local populations until the last-remaining population—therefore the species—went extinct<sup>27</sup>. Given that the  $C_3$  component of the vegetation preferred by *P. robustus* was never dominant in the landscape, even during humid periods, populations of this species would have been especially prone to local extinction during dry periods.



Both the long-term state of aridification and the extreme precessional variability in hydroclimate (Fig. 3) could therefore have contributed to the extinction of *P. robustus*.

### Online content

Any Methods, including any statements of data availability and Nature Research reporting summaries, along with any additional references and Source Data files, are available in the online version of the paper at <https://doi.org/10.1038/s41586-018-0309-6>.

Received: 20 November 2017; Accepted: 25 April 2018;

Published online 9 July 2018.

- Vrba, E. S. Environment and evolution: alternative causes of the temporal distribution of evolutionary events. *S. Afr. J. Sci.* **81**, 229–236 (1985).
- deMenocal, P. B. Plio-Pleistocene African climate. *Science* **270**, 53–59 (1995).
- Potts, R. Environmental hypotheses of hominin evolution. *Yearb. Phys. Anthropol.* **41**, 93–136 (1998).
- Maslin, M. A. & Trauth, M. H. in *The First Humans: Origin and Early Evolution of the Genus Homo* (eds Grine, F. E. et al.) 151–158 (Springer, New York, 2009).
- Cerling, T. E. et al. Woody cover and hominin environments in the past 6 million years. *Nature* **476**, 51–56 (2011).
- Blumenthal, S. A. et al. Aridity and hominin environments. *Proc. Natl Acad. Sci. USA* **114**, 7331–7336 (2017).
- Lyons, R. P. et al. Continuous 1.3-million-year record of East African hydroclimate, and implications for patterns of evolution and biodiversity. *Proc. Natl Acad. Sci. USA* **112**, 15568–15573 (2015).
- Johnson, T. C. et al. A progressively wetter climate in southern East Africa over the past 1.3 million years. *Nature* **537**, 220–224 (2016).
- Partridge, T. C., Demenocal, P. B., Lorentz, S. A., Paiker, M. J. & Vogel, J. C. Orbital forcing of climate over South Africa: a 200,000-year rainfall record from the Pretoria saltpan. *Quat. Sci. Rev.* **16**, 1125–1133 (1997).
- Schefuß, E., Kuhlmann, H., Mollenhauer, G., Prange, M. & Pätzold, J. Forcing of wet phases in southeast Africa over the past 17,000 years. *Nature* **480**, 509–512 (2011).
- Simon, M. H. et al. Eastern South African hydroclimate over the past 270,000 years. *Sci. Rep.* **5**, 18153 (2015).
- Tierney, J. E. et al. Northern Hemisphere controls on tropical southeast African climate during the past 60,000 years. *Science* **322**, 252–255 (2008).
- Dupont, L. M. et al. Glacial–interglacial vegetation dynamics in South Eastern Africa coupled to sea surface temperature variations in the Western Indian Ocean. *Clim. Past* **7**, 1209–1224 (2011).
- Schefuß, E., Schouten, S. & Schneider, R. R. Climatic controls on central African hydrology during the past 20,000 years. *Nature* **437**, 1003–1006 (2005).
- Caley, T. et al. High-latitude obliquity as a dominant forcing in the Agulhas current system. *Clim. Past* **7**, 1285–1296 (2011).
- Castañeda, I. S. et al. Middle to Late Pleistocene vegetation and climate change in subtropical southern East Africa. *Earth Planet. Sci. Lett.* **450**, 306–316 (2016).
- Tyson, P. D. & Preston-Whyte, R. A. *The Weather and Climate of Southern Africa* (Oxford Univ. Press, Oxford, 2000).
- Kutzbach, J. E., Liu, X., Liu, Z. & Chen, G. Simulation of the evolutionary response of global summer monsoons to orbital forcing over the past 280,000 years. *Clim. Dyn.* **30**, 567–579 (2008).
- Reason, C. J. C. Subtropical Indian Ocean SST dipole events and southern African rainfall. *Geophys. Res. Lett.* **28**, 2225–2227 (2001).
- McClymont, E. L., Soudrian, S. M., Rosell-Melé, A. & Rosenthal, Y. Pleistocene sea-surface temperature evolution: early cooling, delayed glacial intensification, and implications for the mid-Pleistocene climate transition. *Earth Sci. Rev.* **123**, 173–193 (2013).
- Elderfield, H. et al. Evolution of ocean temperature and ice volume through the mid-Pleistocene climate transition. *Science* **337**, 704–709 (2012).
- Pollard, D. & DeConto, R. M. Modelling West Antarctic ice sheet growth and collapse through the past five million years. *Nature* **458**, 329–332 (2009).
- Tierney, J. E., Smerdon, J. E., Anchukaitis, K. J. & Seager, R. Multidecadal variability in East African hydroclimate controlled by the Indian Ocean. *Nature* **493**, 389–392 (2013).
- Balter, V., Braga, J., Télouk, P. & Thackeray, J. F. Evidence for dietary change but not landscape use in South African early hominins. *Nature* **489**, 558–560 (2012).
- Henry, A. G. et al. The diet of *Australopithecus sediba*. *Nature* **487**, 90–93 (2012).
- Zliobaitė, I., Fortelius, M. & Stenseth, N. C. Reconciling taxon senescence with the Red Queen's hypothesis. *Nature* **552**, 92–95 (2017).
- Foley, R. in *African Biogeography, Climate Change, and Human Evolution* (eds Bromage, T. G. & Schrenk, F.) 328–348 (Oxford Univ. Press, Oxford, 1999).
- Xie, P. & Arkin, P. A. Global precipitation: a 17-year monthly analysis based on gauge observations, satellite estimates and numerical model outputs. *Bull. Am. Meteorol. Soc.* **78**, 2539–2558 (1997).
- Locarnini, R. A. et al. *World Ocean Atlas 2009. Volume 1: Temperature* (NOAA Atlas NESDIS 68, U.S. Government Printing Office, Washington, D.C., 2010).
- Still, C. J. & Powell, R. L. in *Isoscapes: Understanding Movement, Pattern, and Process on Earth through Isotope Mapping* (eds West, J. B. et al.) 179–194 (Springer, Dordrecht, 2010).
- Laskar, J. et al. A long-term numerical solution for the insolation quantities of the Earth. *Astron. Astrophys.* **428**, 261–285 (2004).

**Acknowledgements** T.C. is supported by CNRS-INSU. Funding from LEFE-IMAGO CNRS INSU project SeaSalt is acknowledged. T.C. was partly supported by the 'Laboratoire d'Excellence' LabexMER (ANR-10-LABX-19) and co-funded by a grant from the French government under the program 'Investissements d'Avenir', and by a grant from the Regional Council of Brittany (SAD programme). J.A.C. acknowledges funding from the ERC project 'STEEPCLIM'. E.S. and L.D. acknowledge funding through the DFG Research Center/Cluster of Excellence 'The Ocean in the Earth System' at MARUM – Center for Environmental Sciences. A.S. acknowledges funding through the LaScArBx, a programme supported by the Agence Nationale de la Recherche (ANR-10-LABX-52). C.G.-C. was supported by CREST (grant number JPMJCR12A3; P.I. SLS) funded by the Japan Science and Technology (JST). Core MD96-2048 was collected during the MOZAPHARE cruise of the RV Marion Dufresne, supported by the French agencies Ministère de l'Éducation Nationale de la Recherche et de la Technologie, Centre National de la Recherche Scientifique (CNRS) and Institut Paul Emile Victor (IPEV).

**Reviewer information** Nature thanks C. O'Brien, M. Petraglia, K. Uno and the other anonymous reviewer(s) for their contribution to the peer review of this work.

**Author contributions** T.C. designed the study. T.C., T.E., M.W. and P.-Y.G. performed the Mg/Ca measurements. L.R. analysed the foraminifera assemblages, and T.C. and F.E. analysed the results and performed the transfer function. T.C., T.E., B.M. and K.C. performed the  $\delta^{18}\text{O}$  analyses on foraminifera. T.C., J.G., P.M. and I.B. performed the XRF measurements and F.J.J.-E. and C.G.-C. conducted the statistical analyses on XRF. J.A.C. and E.S. performed plant-wax  $\delta\text{D}$  and  $\delta^{13}\text{C}$  analyses. L.D. performed the pollen analysis. A.S. and T.C. produced the synthesis on the ecology and environments of South African hominins and conducted the comparisons to the marine record. T.C. and D.M.R. performed and analysed the iLOVECLIM model results. T.C. analysed the results and all authors participated in the interpretation. T.C. wrote the manuscript with contributions from all authors.

**Competing interests** The authors declare no competing interests.

### Additional information

**Extended data** is available for this paper at <https://doi.org/10.1038/s41586-018-0309-6>.

**Reprints and permissions information** is available at <http://www.nature.com/reprints>.

**Correspondence and requests for materials** should be addressed to T.C.

**Publisher's note:** Springer Nature remains neutral with regard to jurisdictional claims in published maps and institutional affiliations.

## METHODS

**XRF measurements.** Element intensities were measured using a XRF-Avaatech core scanner at EPOC. Before analysis, the sediment surface was flattened and covered with Ultralene film. The core sections were scanned at a 0.5-cm resolution at two different levels of energy (10 and 30 keV).

To easily identify periods in XRF  $\ln(\text{Fe}/\text{Ca})$  record, we computed the cumulative sum (csum) of the deviations from the mean:  $\text{csum} = \text{sum}(\ln(\text{Fe}/\text{Ca}) - (\text{mean}(\ln(\text{Fe}/\text{Ca})))$ . The cumulative sum method was developed for industrial control to detect changes in sequential production<sup>32</sup>. More recently, the cumulative sum has been extensively applied in biological oceanography (for example, ref. <sup>33</sup>) following ref. <sup>34</sup>. We first confirmed the regularity of our time series—no periods with greater sampling effort; the average sampling effort was 283 years with only 8% of scattered time gaps greater than 500 years—and ensured that our periodicity matched that of regularized time series at 500-year and 1,000-year windows. The cumulative sum shows periods (that is, linear sequences) and their value with respect to the long-term average: a positive slope shows a period of values greater than the long-term average, and a negative slope shows a period of values smaller than the long-term average. The steepness of the slope reflects how different a period is from the long-term average. Furthermore, changes in the tendency (that is, sequential periodical changes in the slope) reflect periodical changes from a set of conditions to another (for example, a change from a positive slope to a flat slope in the XRF  $\ln(\text{Fe}/\text{Ca})$  record reflects a change from a humid period to a drier period). In the case of the 1–0.6-Ma interval, this corresponds to a period of aridification because it is more arid than the previous period between 1.2 Ma and 1 Ma (that is, there is a change of slope from steeply positive to slightly negative). In addition, the period between 1 Ma and 0.6 Ma is very variable, because the slope is noisy rather than straight. The cumulative sum can be found under the function name *local.trend*, in the R package *Pastecs* (package of analysis of space-time ecological series).

**Plant-wax  $\delta\text{D}$  and  $\delta^{13}\text{C}$ .** Plant-wax analyses were carried out at MARUM. Samples were oven dried at 40 °C, homogenized and squalane was added as an internal standard before extraction. Lipids were extracted with a DIONEX accelerated solvent extractor using a 9:1 mixture of dichloromethane to methanol at 100 °C and 1,000 p.s.i. for five minutes, repeated three times. The saturated hydrocarbon fraction was obtained by elution of the dried lipid extract over a silica column with hexane and subsequent elution over  $\text{AgNO}_3$ -coated silica to remove unsaturated hydrocarbons.

Compound-specific stable carbon isotope ( $\delta^{13}\text{C}$ ) analyses were carried out using a Thermo Fisher Scientific Trace GC Ultra coupled to a Finnigan MAT 252 isotope-ratio-monitoring mass spectrometer via a combustion interface operated at 1,000 °C. Isotope values were calibrated against external  $\text{CO}_2$  reference gas and are reported as parts per thousand (‰) against the Vienna Pee Dee Belemnite (V-PDB) standard. Samples were run in at least duplicate. The internal standards yielded a precision of  $\leq 0.3\text{‰}$ . Repeated analysis of an external *n*-alkane standard between samples yielded a root-mean-squared accuracy of 0.1‰ and a standard deviation of on average 0.2‰.

When possible, given the high amount of lipids necessary, compound-specific stable hydrogen isotope ( $\delta\text{D}$ ) compositions were measured using a Thermo Fisher Scientific Trace GC coupled via a pyrolysis reactor operated at 1,420 °C to a Thermo Fisher MAT 253 isotope-ratio mass spectrometer.  $\delta\text{D}$  values were calibrated against external  $\text{H}_2$  reference gas, the  $3\text{H}+$  factor was monitored daily (values vary between 6.7 and 6.9);  $\delta\text{D}$  values are reported in parts per thousand (‰) versus the Vienna Standard of Mean Ocean Water (VSMOW) standard. The internal standards yielded a precision of 2‰ on average. Repeated analysis of an external *n*-alkane standard between samples yielded a root-mean-squared accuracy of  $<1\text{‰}$  and a standard deviation of on average 3‰.

The results of a method to adjust the  $\delta\text{D}_{\text{wax}}$  record for vegetation and ice-volume changes are given in Extended Data Fig. 4.

**Pollen preparation.** Samples of 1.5 to 8.5 ml were prepared at MARUM. The volume was measured using water displacement. Samples were decalcified with diluted HCl (~12%) and treated with HF (~40%) to remove silicates. Samples were sieved over a screen to remove particles smaller than 10–12  $\mu\text{m}$ . When necessary the sample was decanted to remove remaining silt. Samples were stored in water, mounted in glycerol and microscopically examined (magnification 400 $\times$  and 1,000 $\times$ ) for pollen and spores. Cyperaceae (sedges) pollen percentages were calculated based on the total number of pollen and spores, ranging from 53 to 365, and 95% confidence intervals were calculated according to a previously published method<sup>35</sup>.

**$\delta^{18}\text{O}$  analyses on foraminifera.** Specimens of benthic *Planulina wuellerstorfi* foraminifera were picked from the 250–315- $\mu\text{m}$  size fraction. Analyses were carried out by a coupled system Multiprep–Optima of Micromass at EPOC. The automated preparation system (Multiprep) transforms carbonate samples into  $\text{CO}_2$  gas by treatment with orthophosphoric acid at a constant temperature of 75 °C. The  $\text{CO}_2$  gas samples were then analysed by isotope mass spectrometry (Optima) in comparison with a calibrated reference gas to determine the isotopic ratio  $^{18}\text{O}/^{16}\text{O}$

of the sample. For all stable oxygen isotope measurements a working standard (Burgbrohl  $\text{CO}_2$  gas) was used, which was calibrated against the Vienna Pee Dee Belemnite (V-PDB) standard by using the NBS 19 standard. Analytical standard deviation is about 0.05‰ ( $\pm 1\sigma$ ).

The chronology of the core was established by tuning the  $\delta^{18}\text{O}$  benthic foraminifera signal to the reference LR04 stack<sup>36</sup> with the *AnalySeries* software<sup>37</sup> and yielded a correlation coefficient of  $R = 0.8$  for the past 2.14 Myr. The core is about 36 m long and the sedimentation rate has a mean value of 2 cm per kyr ( $\sigma = 0.91$ ) and is relatively constant.

**SSTs reconstruction.** *Globigerinoides ruber sensu stricto* were picked within the 250–315- $\mu\text{m}$  size fraction for trace element analyses. Shells were cleaned at EPOC to eliminate contamination by clays and organic matter based on a previously published procedure<sup>38</sup>. An Agilent inductively coupled plasma optical emission spectrometer (ICP-OES) was used for magnesium and calcium analyses following a previously established procedure<sup>39</sup>. Reproducibility obtained from *G. ruber s. s.* on 80 samples from the complete core was better than 6% ( $\pm 1\sigma$ , pooled standard deviation). All new analyses for this study ( $n = 217$ ) were performed at EPOC. Measured Mg/Ca ratios were converted into temperature values applying a previously established equation<sup>40</sup>, yielding a precision of 1.2 °C.

Total assemblages of planktonic foraminifera were analysed at EPOC using an Olympus SZH10 binocular microscope following previously published taxonomy<sup>41,42</sup>. About 300 specimens were counted in each level after splitting with an Otto microsplitter. Relative abundances of species were used to perform quantification of SST after an ecological transfer function<sup>43</sup> developed at EPOC. The method used here is based on the modern analogue techniques<sup>44</sup> running under the R software, using the *ReconstMAT* script developed by J. Guiot (BIOINDIC package, <https://www.eccorev.fr/spip.php?article389>). The modern database used is composed of 367 core tops and derived from core tops covering the southern Indian Ocean<sup>45</sup> in the MARGO project. Calculations of past hydrological parameters rely on a weighted average of SST values from the best five modern analogues, with a maximum weight given to the closest analogue in terms of statistical distance (that is, dissimilarity minimum)<sup>43,46</sup>. This method permits the reconstruction of annual SST with a precision of 0.8 °C (Extended Data Fig. 7).

As each proxy has some uncertainty related to the calibration, non-temperature influences and lateral advection<sup>15</sup>, we applied empirical orthogonal function analysis<sup>47</sup> to the two SST records for the past 2.14 Myr (Extended Data Fig. 6). The first principal component (PC1) explains 74% of the total variance for the Mg/Ca and foraminifera transfer function records over the past 2.14 Myr. The correlation between SST proxies and PC1 over the past 2.14 Myr is  $R = 0.71$ .

**Climate modelling.** To investigate the control on the past  $\delta\text{D}$  composition of precipitation in the Limpopo catchment, we analysed the results of a transient run with the intermediate complexity isotope-enabled climate model iLOVECLIM<sup>48–50</sup> over the past 150 kyr<sup>51</sup>. The atmospheric part of the coupled climate model was run at T21 spatial resolution<sup>51</sup> (~5.65° latitude and longitude) and used accelerated forcing (irradiance, greenhouse gases and ice sheets were updated with an acceleration factor 10). Intermediate complexity models experience some weaknesses caused by the spatial resolution and simplified convective physics but have the advantage of efficient computation. iLOVECLIM was previously successfully applied in the Asian monsoon region<sup>51</sup> and in the West African monsoon region<sup>52</sup> to investigate past monsoonal precipitation changes and their links with changes in the isotopic composition of precipitation. For the current study, analysis of the present-day performance of the iLOVECLIM model for the region, together with results over the past 150 kyr, are shown in Extended Data Fig. 2.

**Ecology and environment of the hominins *P. robustus* and *A. sediba* in the Limpopo catchment.** Building on previous research<sup>53,54</sup>, we produce a short synthesis of multiple lines of evidence to reconstruct the ecology and environmental context of the southern African robust australopith *P. robustus*. We also briefly discuss *A. sediba*. Much literature has been devoted to the ecology of the robust australopiths, and particularly to the ecological differences between *P. robustus* and *P. boisei*, another species that is found in eastern Africa. Given that our geographic scope is centred on South Africa, we here focus mostly on *P. robustus*. It remains a matter of debate whether the robust australopiths—*P. robustus*, *P. boisei* and *P. aethiopicus* (the probable ancestor of *P. boisei*, also found in eastern Africa)—are closely related to each other in a monophyletic genus or whether robust adaptive traits evolved independently by convergence or parallelism in eastern Africa and southern Africa, which would make the *Paranthropus* genus diphyletic<sup>54,55</sup>. Authors who support the diphyletic hypothesis tend to classify the robust australopiths in the genus *Australopithecus*. Until the issue is settled, here we use the genus name *Paranthropus* as a convenient taxonomic label of a grade that groups these three taxa, which share similar robust adaptive features that differ from the more-gracile genera *Australopithecus* and *Homo*.

**Cranio-mandibular and dental morphology.** Species of *Paranthropus* are characterized by a suite of cranio-mandibular and dental morphological characters: reduced incisors and canines, molarized premolars, enlarged molars, thick

enamel, enlarged insertion areas for temporal muscles and a robust mandibular corpus<sup>56</sup>. This suite of robust morphological traits has been frequently interpreted as potential adaptations to diets including hard foods<sup>57,58</sup>. This interpretation is partly supported in *P. robustus* by dental microwear data that indicate occasional consumption of hard objects (see below). Other authors have suggested that these characters reflect the ability of *Paranthropus* to chew tough plant matter for prolonged periods<sup>59,60</sup>. This alternative interpretation is supported by dental microwear and stable carbon isotopic data in *P. boisei*<sup>61,62</sup>. This interpretation could apply to *P. robustus* as well, even though this species probably fed on different kinds of plants to those eaten by *P. boisei* ( $C_4$  herbaceous plants in *P. boisei* versus various  $C_3$  and  $C_4$  plants in *P. robustus*, see below).

Potential modern analogues of herbivorous mammals that evolved from omnivorous ancestors that have thick enamel and bunodont molars include the giant panda *Ailuropoda melanoleuca* and the red panda *Ailurus fulgens*, both of which have independently become highly specialized on a diet of tough bamboo leaves that require prolonged chewing and numerous repeated chewing cycles<sup>63,64</sup>. Both examples illustrate phylogenetic inertia, with evolution acting on preexistent morphologies that limit the range of possible adaptive traits in response to functional selective pressure and result in seemingly suboptimal morphologies for the realized diet. A similar argument has been made for *Paranthropus*<sup>53,65</sup>. Therefore, contrary to herbivorous ungulates that evolved long shearing crests and a more lateral mastication to reduce plant matter into small digestible fragments, the giant panda, the red panda and *Paranthropus* evolved alternative solutions combining thick enamel and increased dental surface with prolonged use of high masticatory forces.

It has also been suggested that an increased dental occlusal surface in mammals could be an adaptive trait for feeding on small bites of small-sized food items<sup>66</sup> by increasing the chance of efficiently masticating the food items with a reduced number of chewing cycles, and limiting the wear induced by a strong increased attrition (tooth-to-tooth contact) in addition to the wear induced by abrasion (tooth-to-food contact). Similar adaptive traits, most notably enlarged surfaces of third molars, evolved independently multiple times in African herbivorous suids<sup>67</sup>.

Compared to *Paranthropus*, the craniomandibular and dental morphology of *A. sediba* is more gracile and more similar to that found in older species of *Australopithecus* and younger species of *Homo*. It has recently been argued that the morphology of the cranium was unsuited for feeding on hard objects<sup>68</sup>, but that the morphology of the mandible was suited for this activity<sup>69</sup>.

**Postcranial morphology.** Very little is known about the postcranial morphology of *P. robustus* but most studies indicate the retention of traits adaptive for arboreal climbing<sup>70,71</sup>. Hand morphology suggests an ability to perform precision gripping during tool-making and tool-using activities<sup>72</sup>. Numerous bone tools are found in Swartkrans member 3 and Drimolen, sites that have yielded numerous specimens of *P. robustus*. Microscopic and macroscopic wear analyses as well as experimental data suggest that these tools were used for digging into termite mounds<sup>73–75</sup>. The scarcity of *Homo* remains compared to those of *P. robustus* in sites bearing bone tools suggests that the latter species is most likely to be the tool maker and user<sup>73–75</sup>. *A. sediba* is known by two partial skeletons that provide much information on its postcranial morphology. The upper limbs and shoulders of this species retained numerous adaptive traits for climbing and suspensory behaviours<sup>76,77</sup>.

**Microstructure and biomechanics of enamel.** A study of the dental microstructure of *P. robustus* indicates that its enamel was decussated (contrary that of *P. boisei*<sup>78</sup>), which is assumed to reflect a capacity to withstand strong and/or prolonged biomechanical constraints during mastication. Other mammals that feed on hard objects, such as hyaenids<sup>79</sup>, and mammals that feed on tough vegetation, such as many ungulates, also display decussated enamel<sup>80</sup>.

In addition, an experimental study of the behaviour of enamel under various biomechanical constraints suggests that thick enamel could be an adaptive trait to deal with foods that are either hard or tough, or laden with particulates, potentially including both grit and phytoliths<sup>81</sup>. A recent study observed a low frequency of enamel chipping in *P. robustus*, concluding that it was adapted to eating tough vegetation rather than hard foods<sup>82</sup>. This interpretation is at odds with the dental microwear data that indicate at least some consumption of hard objects (see 'Dental microwear'). Alternatively, we argue that it is equally plausible that this low frequency of chipping is related to the specialized decussated microstructure that reinforces the tooth enamel of *P. robustus* at a microscopic scale, making its teeth less prone to chipping and therefore more durable when consuming hard or tough foods.

**Enamel biogeochemistry.** Numerous data are available regarding the stable carbon and oxygen isotopic compositions (expressed as  $\delta^{13}C$  and  $\delta^{18}O$ , respectively) and the major elements (Sr, Ba and Ca) of the enamel of *P. robustus*, of other hominins and of other contemporaneous animals. The stable carbon isotope ratios enable the quantification of the proportions of food items deriving, directly or indirectly (through one or several trophic levels), from  $C_3$  plants (mostly woody vegetation, but also sedges in humid environments) and  $C_4$  plants (mostly grass and sedges, but also shrubs of the *Amaranthaceae* and *Chenopodiaceae* family). The  $\delta^{13}C$  values of

the enamel of *P. robustus* indicate a diet that was dominated by foods derived from  $C_3$  plants, with a substantial proportion (about 35–40%) of foods derived from  $C_4$  plants (Fig. 3f and Extended Data Table 2). Much effort has been dedicated to identifying the food items that compose this substantial  $C_4$  component in the diet of *P. robustus*<sup>83–86</sup>. The most probable  $C_4$ -plant-derived food items include grass leaves and roots, insects such as grasshoppers and termites, and small vertebrates (birds, lizards, rodents and small ungulates) that consume either  $C_4$  plants or invertebrates that eat  $C_4$  plants. Sedges are also considered to be a likely source of  $C_4$  resources, notably through the consumption of their underground storage organs (USOs)<sup>87,88</sup>. A previous study<sup>84</sup>, however, has argued that  $C_4$  sedges were rather scattered in South African riverine settings and that not many of them produced large palatable underground storage organs. This study therefore suggested that  $C_4$  sedges represented only a minor food resource for hominins. However, they only studied the sedges from four riverine sites located in the Kruger National Park and it remains unknown whether their conclusions are valid for the whole Limpopo catchment and larger scales.

More important in our opinion is the fact that the diet of *P. robustus* was dominated by  $C_3$ -plant-derived food resources, which could include any parts (leaves, stems, fruits, nuts or underground storage organs) of  $C_3$  plants (mostly trees, shrubs and bushes in wooded environments but also abundant sedges in humid environments). There is little data on the enamel  $\delta^{13}C$  values of *A. sediba* ( $n=2$ ) but both specimens display low values ( $-12.1\%$  and  $-12.2\%$ ) that indicate a diet dominated by  $C_3$ -plant-derived food resources<sup>25</sup>.

Stable oxygen ratios of enamel are related to multiple factors, including behaviour, ecology, diet, physiology and climate<sup>89</sup>. A previous study<sup>90</sup> classified mammals into evaporation sensitive and evaporation insensitive taxa. The  $\delta^{18}O$  values in evaporation sensitive taxa increase with aridity. Evaporation sensitive taxa do not drink much and get most of the water they require from the plants they consume. Conversely,  $\delta^{18}O$  values of evaporation insensitive taxa track the  $\delta^{18}O$  values of surface water that they drink abundantly and frequently<sup>90,91</sup>. Although hominins were not included in this classification scheme, they are probably water-dependent, as all large primates need to drink a lot of water every day. Hominins generally display relatively low  $\delta^{18}O$  values on average compared to the rest of the fauna<sup>62,92</sup>, suggesting a high water dependence or consumption of plants containing little evaporated water. Those data support the preference of *P. robustus* for wooded and/or humid environments.

Intra-tooth variations of  $\delta^{13}C$  and  $\delta^{18}O$  also provide information about intra-annual and inter-annual variation in ecology. Intra-tooth  $\delta^{13}C$  and  $\delta^{18}O$  profiles were measured using laser ablation on four teeth of *P. robustus* from Swartkrans member 1<sup>83</sup>. The mean values of the  $\delta^{13}C$  profiles are similar to those of other *P. robustus* individuals sampled previously, and they also reveal substantial intra-tooth variation with ranges varying from 2‰ to 5‰ over periods representing approximately one or two years (inferred from the number of perikymata). Significant positive correlations between the  $\delta^{13}C$  and  $\delta^{18}O$  in three out of four specimens of *P. robustus* also indicate that they consumed relatively more  $C_4$ -plant-derived foods during the dry season than during the wet season<sup>83</sup>. This could suggest an opportunistic sampling of the environment, with a relative consumption of foods derived from  $C_3$  or  $C_4$  plants that depended in part on seasonal or inter-annual climatic differences. These data are also congruent with the identification of *P. robustus* as an evaporation insensitive taxon and are similar to the pattern observed in some extant evaporation insensitive herbivorous ungulates (for example, strong positive correlations of  $\delta^{13}C$  and  $\delta^{18}O$  profiles in an extant common hippopotamus *Hippopotamus amphibius*<sup>93</sup>).

Investigations of trace elements preserved in the enamel of *P. robustus* have also revealed interesting patterns<sup>24,94</sup>. *P. robustus* is characterized by relatively high Sr/Ca ratios, lower than in grazing ungulates and slightly higher than in carnivores, browsing ungulates and omnivorous cercopithecoid monkeys. *Australopithecus africanus* is characterized by even higher Sr/Ca ratios. Both hominins, but especially *A. africanus*, display low Ba/Ca ratios. Altogether, these data indicate that the proportion of animal matter in their diets is likely to have been low. The only extant animals that combine a high Sr/Ca ratio and a low Ba/Ca ratio are the mole rat (*Cryptomys hottentotus*), and to a lesser extent, the common warthog (*Phacochoerus africanus*). Both species consume large amounts of grass roots. This could indicate that grass root consumption was an important aspect of the diet of *P. robustus*, explaining part of the  $C_4$  component of the diet. However, the Sr/Ca and the Ba/Ca ratios of *A. africanus* and *P. robustus* are not as extreme as those found in the mole rat and the common warthog, suggesting that the consumption of grass roots was probably not as important as in those two species. As previously highlighted<sup>94</sup>, one must, however, stress that the use of major element concentrations in enamel as an indication of the diet of extant and extinct animals still require further study. One previous study<sup>24</sup> observed Sr/Ca and Ba/Ca ratios for *P. robustus* that are intermediate between those of *A. africanus* and early *Homo*, and similar to those of browsers: these authors argue the diet of *P. robustus* was dominated by woody plants.



**Dental microwear.** Investigations of dental microwear have also provided useful information for reconstructing the diet of *P. robustus*<sup>61,95–97</sup>. Dental microwear mostly results from a combination of abrasion (food-to-tooth contact) and attrition (tooth-to-tooth contact), both of which result in various microscopic scars left at the surface of the enamel facets. Among hominins, specimens of *P. robustus* are characterized by unique microwear textures that display strongly variable complexities, ranging from low to very high values, and low anisotropies. This pattern, originally observed on a few specimens, was later confirmed by a large-scale study of dental microwear in *P. robustus*, including numerous specimens from various sites<sup>98</sup>. Similarities in dental microwear textures were noted between *P. robustus* and specimens of several extant primates that are known to consume hard objects such as nuts and seeds (grey-cheeked mangabeys, *Lophocebus albigena* or brown capuchins, *Sapajus apella*), indicating at least some consumption of hard objects by *P. robustus*. Dental microwear data available for *A. sediba*—although they are based on only two specimens—also show high complexities, suggesting a potential consumption of hard objects<sup>25</sup>.

**Stable carbon isotopes of contemporary mammals.** Compiled data of  $\delta^{13}\text{C}$  values for herbivorous mammals that were contemporary and sympatric with *P. robustus* indicate habitats encompassing a mix of  $\text{C}_3$  and  $\text{C}_4$  plants, suggesting a mix of woodlands and grasslands in all sites that were sampled (data for Swartkrans members 1, 2, and 3<sup>83,84,99,100</sup>; Cooper's Cave D<sup>101</sup>; Gondolin<sup>102</sup>; Fig. 3f and Extended Data Table 2). The enamel  $\delta^{13}\text{C}$  values of herbivorous mammals contemporaneous with *P. robustus* from all sites for which sufficient data are available display a bimodal distribution (Extended Data Table 2): the main mode indicates that the habitat was dominated by herbivorous mammals consuming mostly  $\text{C}_4$  plants, and the secondary mode indicates that a substantial portion of the remaining herbivorous mammals consumed  $\text{C}_3$  plants. Mammals displaying a strong  $\text{C}_4$  signal in their enamel probably consumed herbaceous plants, including mostly dry-adapted  $\text{C}_4$  grasses in open habitats and possibly  $\text{C}_4$  sedges in humid habitats. They are usually classified as grazers. Conversely, mammals displaying a strong  $\text{C}_3$  signal in their enamel probably fed mainly on woody plants (trees, shrubs or bushes) in woodlands, and possibly on  $\text{C}_3$  sedges in humid habitats. They are usually classified as browsers. Complicating factors of palaeodietary reconstructions include the potential consumption of CAM plants (mostly succulents in arid habitats, and epiphytic plants in closed forests) and  $\text{C}_4$  dicot woody vegetation (for example, shrubs of the family Amaranthaceae or Chenopodiaceae). However, the classification of mammals using the dichotomy between  $\text{C}_3$  browsers and  $\text{C}_4$  grazers inferred from  $\delta^{13}\text{C}$  values is generally confirmed by ecomorphological and dental wear studies<sup>101</sup>.  $\delta^{13}\text{C}$  data of *P. robustus* are intermediate between the  $\text{C}_4$  pole and the  $\text{C}_3$  pole, but closer to the latter, indicating a preference of this hominin for the  $\text{C}_3$  wooded and/or humid component of its habitat.

The enamel  $\delta^{13}\text{C}$  data of the herbivorous mammals found at the Malapa site with *A. sediba* indicate an environment dominated by  $\text{C}_4$  plants, presumably grasses, and a few species consuming  $\text{C}_3$  plants, presumably woody plants<sup>25</sup>. The pattern is therefore similar to that observed in sites containing *P. robustus*, indicating a preference of *A. sediba* for the  $\text{C}_3$  component—presumably woodland—of the otherwise  $\text{C}_4$ -grass-dominated landscapes.

**Ecomorphology and community structures.** A previous analysis<sup>103</sup> quantified trophic and locomotor adaptive traits of mammals to compare the ecological diversity of modern and past faunal communities, and found evidence that *P. robustus* inhabited mosaic environments that included both woodlands and grasslands, always close to a water source. This study also detected a pattern of more-open habitats throughout the Swartkrans sequence. This observation supports the information provided by  $\delta^{13}\text{C}$  values of the herbivorous mammals that—based on our data compilation—generally indicate more  $\text{C}_4$  plants in the landscape, presumably grasses adapted to open and dry environments (Fig. 3f). Another previous study<sup>104</sup> conducted a correspondence analysis using the relative abundances of the different groups of mammals classified as woodland-adapted and grassland-adapted, on the basis of stable carbon isotopes and uniformitarian comparisons to extant relatives. This study observed that the relative abundance of *P. robustus* follows the relative abundances of woodland-adapted species and is negatively correlated to the relative abundances of grassland-adapted species. An ecomorphological analysis (L. C. Bishop et al., personal communication) of bovid postcrania from Sterkfontein member 5B 'Oldowan infill' concluded that most bovid species were adapted to open grasslands, and reconstructed the environment as dominated by grasslands but with a nearby more-wooded component. Finally, another previous analysis<sup>106</sup> has suggested that the absence of *P. robustus* in Sterkfontein member 5 west could be linked to a drier local habitat without water-dependent species. Overall, these studies indicate that grasslands were important and probably predominant in the environments occupied by *P. robustus*, but always with a more-wooded and humid component nearby. The ecological data gained from multiple lines of evidence suggest that *P. robustus* preferred this woodland and/or humid component.

**Combining the multiple lines of evidence.** Based on the evidence discussed above, we interpret *P. robustus* as a species that was tolerant of environmental

variability (eurytopic), especially in terms of dietary resources, but with a long-lasting preference for the wooded or humid components (characterized by  $\text{C}_3$  plants) of environments that were otherwise dominated by  $\text{C}_4$  dry-adapted plants. Such a selective feeding behaviour—with scarce components of the vegetation that are over-represented in the diet of an animal—is frequently observed in extant mammals. For example, extant geladas (*Theropithecus gelada*) from the Guassa Plateau in the highlands of Ethiopia rely extensively on forbs (about 38% of annual diet, and up to 61% of monthly diet) although their preferred forbs represent only 8% of ground cover<sup>107</sup>. A variable  $\text{C}_3$ -plant-dominated diet, including both hard and tough food items, and displaying strong seasonal or inter-annual variations, is supported by the stable carbon and oxygen isotopes, the dental microwear textures and the overall morphological adaptive traits displayed by *P. robustus*. The robust craniomandibular and dental traits appear as a reasonable compromise to efficiently process an extremely diversified diet including numerous tough parts of plants along with some hard foods, and probably a large number of small food items that had to be eaten in small bites, with some exogenous grit particulates adhering (for example, termites or grass roots).

The preference of *P. robustus* for habitats dominated by  $\text{C}_3$  plants, either in woodlands or in humid environments, is well corroborated by the data gained from the study of other animals, indicating large quantities of  $\text{C}_4$  vegetation but always with a more wooded component and the nearby presence of a water source. Frequent exploitation of the  $\text{C}_4$ -plant food resources in the more open component of the landscapes is demonstrated by stable carbon isotopes that indicate a substantial, but not dominant,  $\text{C}_4$  component in the diet. Prehensile hands and the possible use of bone tools would have enabled *P. robustus* to access a great variety of foods in both wooded and open habitats. *P. robustus* may be best characterized as an ecotonic species, exploiting intermediate habitats in which the edge effect is maximized, enabling it to forage on a maximal variety of foods in both wooded and open habitats within a limited area while retaining access to secure shelters in woodlands. Such an ecology is displayed by the forest hog (*Hylochoerus meinertzhageni*) that strongly depends on wooded humid forests for shelter, food and water, but which also frequently exploits open grasslands for additional plant resources<sup>108</sup>. Data are scarcer for *A. sediba* but the multiple lines of evidence discussed above suggest an even stronger preference for  $\text{C}_3$ -plant-dominated wooded habitats, when compared to *P. robustus*. It is worth noting that a similar preference for the  $\text{C}_3$ -plant component, presumably woodlands, in overall  $\text{C}_4$ -grass-dominated landscapes is also documented in several other hominin species from eastern Africa<sup>109,110</sup>.

**Extinction of *P. robustus*.** It appears likely that the last documented occurrence of *P. robustus* is dated about 0.9 Ma, or even later (see Extended Data Table 1). Indeed, multiple lines of dating evidence point to a young age of Swartkrans member 3, probably around 0.9 Ma but possibly as young as 0.6 Ma. It is also worth noting the frequency of artificial range truncation of extinct taxa, often called the Signor and Lipps effect<sup>111</sup>: owing to the imperfect nature of the fossil record, the extinction date of a particular taxon is most probably more recent than the last fossil occurrence of this taxon. Bearing in mind that this caution was formulated on the basis of the near-continuous and precisely dated marine palaeontological record, the Signor and Lipps effect is even more pertinent when considering extinction dates based on the spatio-temporally biased continental fossil record of terrestrial faunas (see details in ref. <sup>112</sup>). This dating uncertainty most probably applies to *P. robustus* as the known geographic distribution of this species is extremely small. Most of the sites that contain *P. robustus* are located within a circle of about 3-km radius, and only Gondolin is located a bit further north, around 25 km from Swartkrans and Sterkfontein. A circle of 12.5-km radius encompassing all the known occurrences of *P. robustus* would therefore represent a distribution area of about 500 km<sup>2</sup>. Large mammals tend to have much larger geographic distributions than 500 km<sup>2</sup>. For comparison, the critically endangered eastern gorilla (*Gorilla beringei*)—the extant species of African great ape that has the smallest geographic distribution—is found over an area of about 70,000 km<sup>2</sup>. Other great apes have much larger distributions (*Gorilla gorilla*, over 700,000 km<sup>2</sup>; *Pan paniscus*: about 156,000 km<sup>2</sup>; *Pan troglodytes*, over 2,600,000 km<sup>2</sup>; all data are from the International Union for Conservation of Nature website, <http://www.iucnredlist.org/>). It is therefore most likely that the real distribution area of *P. robustus* was much larger than the area that is currently sampled by the available fossil record, making the true last occurrence of the species unlikely to be sampled, and the real extinction date of the species probably younger than 0.9 Ma.

The fossil record of South Africa indicates that numerous species became extinct during the Pleistocene. However, the paucity of the record after 1.4 Ma seriously hinders our understanding of the pattern and timing of the extinctions. Middle Pleistocene faunas such as those of Florisbad (about 0.25 Ma) are almost entirely composed of species that are similar to the extant species whereas older faunas (for example, Cornelia at around 1 Ma or Elandsfontein at 1–0.6 Ma) contain a substantial proportion of extinct species (see ref. <sup>113</sup>). Neither a precise date nor a time interval (1–0.5 Ma versus later during the Pleistocene) can be



constrained for the extinction of those species based on their currently available fossil records.

Our marine record and previously published terrestrial records are indicative of a clear trend through time towards more-open and drier landscapes in the Limpopo catchment. Given that *P. robustus* preferentially thrived in the non-dominant component of its environment (either woodland or humid grassland) characterized by  $C_3$  plants, and that the diet of this species was dominated by  $C_3$ -plant-derived food items, including occasional hard objects, we assume that the regional trend towards a more arid hydroclimate after 1 Ma and the marked precessional variability affected the abundance of this species and its resilience to environmental changes. As the regional hydroclimate became drier, the wooded and humid environments favoured by *P. robustus* probably became progressively scarcer, strongly affecting the fitness and survival of populations of mammals that depended on these habitats for food, water and shelter. We propose a speculative, but plausible, scenario inspired by previous theoretical work<sup>27</sup>. According to this scenario, the geographic ranges of taxa adapted to woodlands and humid habitats, including *P. robustus*, contracted and expanded according to the precessional ~21-kyr dry and wet cycles. During multi-millennial dry periods, the range of populations of these taxa contracted and often became fragmented. The resulting isolated populations were especially prone to local extinction through increased competition and predation induced by the lack of sufficient and suitable food, water and shelters. During multi-millennial wet periods, preferred woodland and humid habitats would have expanded again and the surviving populations would have expanded into their previously occupied range, replacing locally extinct populations. The long-term trend to aridity, inferred from our marine record, implies that dry periods became more and more marked through time, increasing the likelihood for local extinction of numerous local populations, until the extinction of the last remaining local population and therefore the extinction of the species. Thus, both long-term state and the extreme precessional changes in hydroclimate could have affected the evolution of *P. robustus*. A recent synthesis of factors involved in the extinction of large mammals—spanning three continents and the whole Cenozoic period—concluded that abiotic changes, such as climatic changes, were key players in the extinctions of species<sup>26</sup>.

**What of *Homo*?** Several authors (reviewed in ref. 114) have suggested that strong morphological, behavioural and ecological differences between *P. robustus* and the contemporary *Homo* gave an evolutionary advantage to the latter over the former. Given that *Homo* did not go extinct and remained extremely widespread in Africa and beyond, some authors have related these differences to the extinction of *P. robustus*. Notably different relative abundances of these two taxa do suggest they were occupying separate ecological niches in the sites where they co-occur (Swartkrans 96% *P. robustus*, 4% *Homo*; Drimolen 84% *P. robustus* 16% *Homo*, according to previous work<sup>115</sup>). However, these scenarios are speculative and clearly beyond the scope of our paper, which is focused on *P. robustus*. Regardless of any potential evolutionary advantage of *Homo* over *P. robustus*, whether or not *Homo* went extinct locally in the Limpopo catchment during the aridification period is meaningless to the subsequent evolutionary history of the genus *Homo*. Remains of *Homo* are known in other parts of South Africa at around 1 Ma (for example, Elandsfontein<sup>116</sup> and Cornelia-Uitzoek<sup>117</sup>), as well as in other parts of Africa<sup>118,119</sup>, which would have made any local extinction counterbalanced by subsequent dispersals from other regions. The survival of *Homo* could plausibly be explained solely through plain contingency, especially as our synthesis as well as recent literature<sup>114</sup> indicates a eurytopic ecology for both *Homo* and *Paranthropus*.

**Code availability.** The iLOVECLIM source code is based on the LOVECLIM model version 1.2, for which code is accessible at <http://www.elic.ucl.ac.be/modx/elic/index.php?id=289>. The developments of the iLOVECLIM source code are hosted at <http://forge.ipsl.jussieu.fr/ludus>, but are not publicly available owing to copyright restrictions. Access can be granted on demand by request to D.M.R. (didier.roche@lsce.ipsl.fr) to those who conduct research in collaboration with the iLOVECLIM users group.

**Data availability.** The datasets generated during and/or analysed during the current study are available from the corresponding author on reasonable request. Source Data for Fig. 2 is provided with the paper.

32. Page, E. S. Continuous inspection schemes. *Biometrika* **41**, 100–115 (1954).

33. García-Comas, C. et al. Zooplankton long-term changes in the NW Mediterranean Sea: decadal periodicity forced by winter hydrographic conditions related to large-scale atmospheric changes? *J. Mar. Syst.* **87**, 216–226 (2011).

34. Ibanez, F., Fromentin, J. M. & Castel, J. Application of the cumulated function to the processing of chronological data in oceanography. *C. R. Acad. Sci. III* **316**, 745–748 (1993).

35. Maher, L. J. Jr. Nomograms for computing 0.95 confidence limits of pollen data. *Rev. Palaeobot. Palynol.* **13**, 85–93 (1972).

36. Lisiecki, L. E. & Raymo, M. E. A Pliocene–Pleistocene stack of 57 globally distributed benthic  $\delta^{18}O$  records. *Paleoceanography* **20**, PA1003 (2005).

37. Paillard, D., Labeyrie, L. D. & Yiou, P. AnalySeries 1.0: Macintosh program performs time-series analysis. *Eos* **77**, 379 (1996).

38. Barker, S., Greaves, M. & Elderfield, H. A study of cleaning procedures used for foraminiferal Mg/Ca paleothermometry. *Geochim. Geophys. Geosyst.* **4**, 8407 (2003).

39. de Villiers, S., Greaves, M. & Elderfield, H. An intensity ratio calibration method for the accurate determination of Mg/Ca and Sr/Ca of marine carbonates by ICP-AES. *Geochim. Geophys. Geosyst.* **3**, 2001GC000169 (2002).

40. Anand, P., Elderfield, H. & Conte, M. H. Calibration of Mg/Ca thermometry in planktonic foraminifera from a sediment trap time series. *Paleoceanography* **18**, 1050 (2003).

41. Hemleben, C., Spindler, M. & Erson, O. R. *Modern Planktonic Foraminifera* (Springer, New York, 1989).

42. Kennett, J. P. & Srinivasan, M. S. *Neogene Planktonic Foraminifera: A Phylogenetic Atlas* (Hutchinson Ross, Stroudsburg, 1983).

43. Guiot, J. & de Vernal, A. in *Proxies in Late Cenozoic Paleoclimatology* (eds Hillaire-Marcel, C. & de Vernal, A.) 523–563 (Elsevier, Amsterdam, 2007).

44. Kucera, M. in *Proxies in Late Cenozoic Paleoclimatology* (eds Hillaire-Marcel, C. & de Vernal, A.) 213–262 (Elsevier, Amsterdam, 2007).

45. Barrows, T. T. & Juggins, S. Sea-surface temperatures around the Australian margin and Indian Ocean during the Last Glacial Maximum. *Quat. Sci. Rev.* **24**, 1017–1047 (2005).

46. Kucera, M. et al. Reconstruction of sea-surface temperatures from assemblages of planktonic foraminifera: multi-technique approach based on geographically constrained calibration data sets and its application to glacial Atlantic and Pacific Oceans. *Quat. Sci. Rev.* **24**, 951–998 (2005).

47. Von Storch, H. & Zwiers, F. W. *Statistical Analysis in Climate Research* (Cambridge Univ. Press, Cambridge, 1999).

48. Roche, D. M.  $\delta^{18}O$  water isotope in the iLOVECLIM model (version 1.0)—part 1: implementation and verification. *Geosci. Model Dev.* **6**, 1481–1491 (2013).

49. Roche, D. M. & Caley, T.  $\delta^{18}O$  water isotope in the iLOVECLIM model (version 1.0)—part 2: evaluation of model results against observed  $\delta^{18}O$  in water samples. *Geosci. Model Dev.* **6**, 1493–1504 (2013).

50. Caley, T. & Roche, D. M.  $\delta^{18}O$  water isotope in the iLOVECLIM model (version 1.0)—part 3: a palaeo-perspective based on present-day data—model comparison for oxygen stable isotopes in carbonates. *Geosci. Model Dev.* **6**, 1505–1516 (2013).

51. Caley, T., Roche, D. M. & Renssen, H. Orbital Asian summer monsoon dynamics revealed using an isotope-enabled global climate model. *Nat. Commun.* **5**, 5371 (2014).

52. Collins, J. A. et al. Rapid termination of the African Humid Period triggered by northern high-latitude cooling. *Nat. Commun.* **8**, 1372 (2017).

53. Grine, F. E. & Daegling, D. J. Functional morphology, biomechanics and the retransition of early hominid diets. *C. R. Palevol* **16**, 613–631 (2017).

54. Wood, B. & Schroer, K. in *Human Paleontology and Prehistory. Contributions in Honor of Yoel Rak* (eds Marom, A. & Hovers, E.) 95–107 (Springer, Cham, 2017).

55. Patterson, D. B., Faith, J. T., Bobe, R. & Wood, B. Regional diversity patterns in African bovids, hyaenids, and felids during the past 3 million years: the role of taphonomic bias and implications for the evolution of *Paranthropus*. *Quat. Sci. Rev.* **96**, 9–22 (2014).

56. Grine, F. E. (ed). *Evolutionary History of the “Robust” Australopithecines* (Aldine de Gruyter, New York, 1988).

57. Strait, D. S. et al. Viewpoints: diet and dietary adaptations in early hominins: the hard food perspective. *Am. J. Phys. Anthropol.* **151**, 339–355 (2013).

58. Smith, A. L. et al. The feeding biomechanics and dietary ecology of *Paranthropus boisei*. *Anat. Rec. (Hoboken)* **298**, 145–167 (2015).

59. Rabenold, D. & Pearson, O. M. Abrasive, silica phytoliths and the evolution of thick molar enamel in primates, with implications for the diet of *Paranthropus boisei*. *PLoS ONE* **6**, e28379 (2011).

60. Scott, J. E., McAbee, K. R., Eastman, M. M. & Ravosa, M. J. Experimental perspective on fallback foods and dietary adaptations in early hominins. *Biol. Lett.* **10**, 20130789 (2014).

61. Ungar, P. S., Grine, F. E. & Teaford, M. F. Dental microwear and diet of the Plio-Pleistocene hominin *Paranthropus boisei*. *PLoS ONE* **3**, e2044 (2008).

62. Cerling, T. E. et al. Diet of *Paranthropus boisei* in the early Pleistocene of East Africa. *Proc. Natl Acad. Sci. USA* **108**, 9337–9341 (2011).

63. King, R. A. Using *Ailuropoda melanoleuca* as a Model Species for Studying the Ecomorphology of *Paranthropus*. MSc. thesis, Marshall Univ. (2014).

64. Weng, Z. Y. et al. Giant panda's tooth enamel: structure, mechanical behavior and toughening mechanisms under indentation. *J. Mech. Behav. Biomed. Mater.* **64**, 125–138 (2016).

65. Ungar, P. S. & Hlusko, L. J. The evolutionary path of least resistance. *Science* **353**, 29–30 (2016).

66. Lucas, P. W. *Dental Functional Morphology: How Teeth Work* (Cambridge Univ. Press, Cambridge, 2004).

67. Souron, A. in *Ecology, Conservation and Management of Wild Pigs and Peccaries* (eds Melletti, M. & Meijaard, E.) 29–38 (Cambridge Univ. Press, Cambridge, 2017).

68. Ledogar, J. A. et al. Mechanical evidence that *Australopithecus sediba* was limited in its ability to eat hard foods. *Nat. Commun.* **7**, 10596 (2016).

69. Daegling, D. J., Carlson, K. J., Tafforeau, P., de Ruiter, D. J. & Berger, L. R. Comparative biomechanics of *Australopithecus sediba* mandibles. *J. Hum. Evol.* **100**, 73–86 (2016).

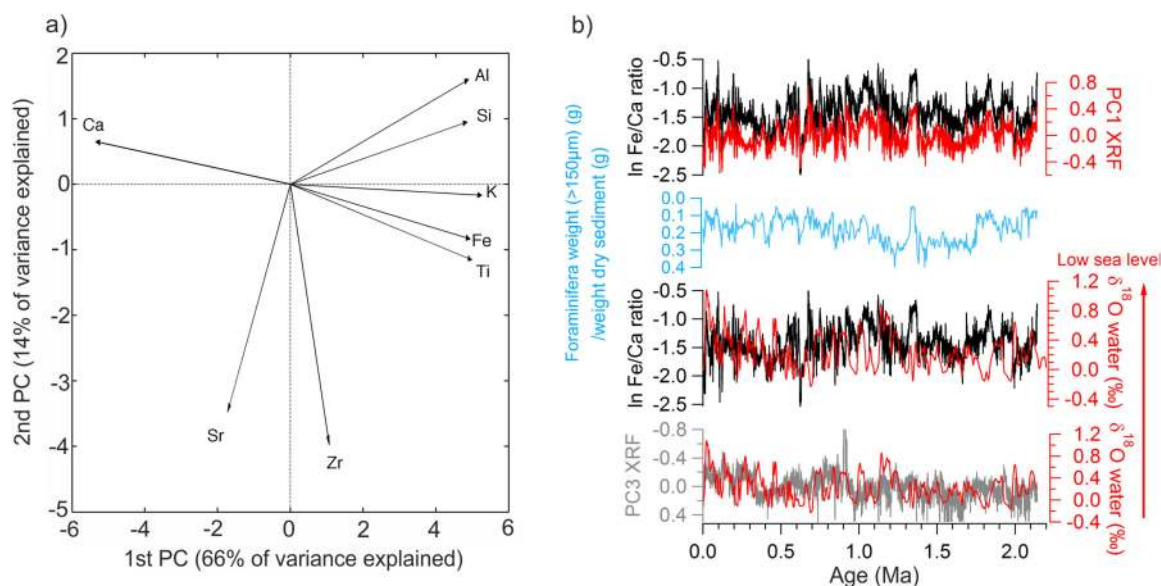
70. Grine, F. E. & Susman, R. L. Radius of *Paranthropus robustus* from member 1, Swartkrans formation, South Africa. *Am. J. Phys. Anthropol.* **84**, 229–248 (1991).

71. Patel, B. A. The hominoid proximal radius: re-interpreting locomotor behaviors in early hominins. *J. Hum. Evol.* **48**, 415–432 (2005).

72. Susman, R. L. Hand of *Paranthropus robustus* from Member 1, Swartkrans: fossil evidence for tool behavior. *Science* **240**, 781–784 (1988).
73. Backwell, L. R. & d'Errico, F. Additional evidence on the early hominid bone tools from Swartkrans with reference to spatial distribution of lithic and organic artefacts. *S. Afr. J. Sci.* **99**, 259–267 (2003).
74. Backwell, L. R. & d'Errico, F. Early hominid bone tools from Drimolen, South Africa. *J. Archaeol. Sci.* **35**, 2880–2894 (2008).
75. d'Errico, F. & Backwell, L. R. Assessing the function of early hominin bone tools. *J. Archaeol. Sci.* **36**, 1764–1773 (2009).
76. Churchill, S. E. et al. The upper limb of *Australopithecus sediba*. *Science* **340**, 1233477 (2013).
77. Rein, T. R., Harrison, T., Carlson, K. J. & Harvati, K. Adaptation to suspensory locomotion in *Australopithecus sediba*. *J. Hum. Evol.* **104**, 1–12 (2017).
78. Macho, G. in *Trends in Biological Anthropology* Vol. 1 (eds Gerdau-Radonić, K. & McSweeney, K.) 1–10 (Oxbow, Oxford, 2015).
79. Tseng, Z. J. Connecting Hunter–Schreger Band microstructure to enamel microwear features: new insights from durophagous carnivores. *Acta Palaeontol. Pol.* **57**, 473–484 (2012).
80. Alloing-Séguier, L. et al. Enamel microstructure evolution in anthracotheres (Mammalia, Cetartiodactyla) and new insights on hippopotamoid phylogeny. *Zool. J. Linn. Soc.* **171**, 668–695 (2014).
81. Constantino, P. J., Borrero-Lopez, O., Pajares, A. & Lawn, B. R. Simulation of enamel wear for reconstruction of diet and feeding behavior in fossil animals: a micromechanics approach. *BioEssays* **38**, 89–99 (2016).
82. Towle, I., Irish, J. D. & De Groote, I. Behavioral inferences from the high levels of dental chipping in *Homo naledi*. *Am. J. Phys. Anthropol.* **164**, 184–192 (2017).
83. Sponheimer, M. et al. Isotopic evidence for dietary variability in the early hominin *Paranthropus robustus*. *Science* **314**, 980–982 (2006).
84. Sponheimer, M. et al. Hominins, sedges, and termites: new carbon isotope data from the Sterkfontein valley and Kruger National Park. *J. Hum. Evol.* **48**, 301–312 (2005).
85. Sponheimer, M. & Lee-Thorp, J. A. Differential resource utilization by extant great apes and australopithecines: towards solving the C<sub>4</sub> conundrum. *Comp. Biochem. Physiol. A* **136**, 27–34 (2003).
86. Sponheimer, M. in *The Paleobiology of Australopithecus* (eds Reed, K. E., Fleagle, J. G. & Leakey, R. E.) 225–233 (Springer, Dordrecht, 2013).
87. Dominy, N. J., Vogel, E. R., Yeakel, J. D., Constantino, P. & Lucas, P. W. Mechanical properties of plant underground storage organs and implications for dietary models of early hominins. *Evol. Biol.* **35**, 159–175 (2008).
88. Yeakel, J. D., Dominy, N. J., Koch, P. L. & Mangel, M. Functional morphology, stable isotopes, and human evolution: a model of consistency. *Evolution* **68**, 190–203 (2014).
89. Sponheimer, M. & Lee-Thorp, J. A. Oxygen isotopes in enamel carbonate and their ecological significance. *J. Archaeol. Sci.* **26**, 723–728 (1999).
90. Levin, N. E., Cerling, T. E., Passey, B. H., Harris, J. M. & Ehleringer, J. R. A stable isotope aridity index for terrestrial environments. *Proc. Natl Acad. Sci. USA* **103**, 11201–11205 (2006).
91. Faith, J. T. Paleodietary change and its implications for aridity indices derived from  $\delta^{18}\text{O}$  of herbivore tooth enamel. *Palaeogeogr. Palaeoclimatol. Palaeoecol.* **490**, 571–578 (2018).
92. Lee-Thorp, J. A., Sponheimer, M., Passey, B. H., de Ruiter, D. J. & Cerling, T. E. Stable isotopes in fossil hominin tooth enamel suggest a fundamental dietary shift in the Pliocene. *Philos. Trans. R. Soc. Lond. B* **365**, 3389–3396 (2010).
93. Souron, A., Balasse, M. & Boissiere, J.-R. Intra-tooth isotopic profiles of canines from extant *Hippopotamus amphibius* and late Pliocene hippopotamids (Shungura Formation, Ethiopia): insights into the seasonality of diet and climate. *Palaeogeogr. Palaeoclimatol. Palaeoecol.* **342–343**, 97–110 (2012).
94. Sponheimer, M., de Ruiter, D., Lee-Thorp, J. & Späth, A. Sr/Ca and early hominin diets revisited: new data from modern and fossil tooth enamel. *J. Hum. Evol.* **48**, 147–156 (2005).
95. Ungar, P. S. & Sponheimer, M. The diets of early hominins. *Science* **334**, 190–193 (2011).
96. Grine, F. E., Sponheimer, M., Ungar, P. S., Lee-Thorp, J. & Teaford, M. F. Dental microwear and stable isotopes inform the paleoecology of extinct hominins. *Am. J. Phys. Anthropol.* **148**, 285–317 (2012).
97. Ungar, P. S., Scott, J. R. & Steininger, C. M. Dental microwear differences between eastern and southern African fossil bovids and hominins. *S. Afr. J. Sci.* **112**, 2015–0393 (2016).
98. Peterson, A. S., Abella, E. F., Grine, F. E., Teaford, M. F. & Ungar, P. S. Microwear textures of *Australopithecus africanus* and *Paranthropus robustus* molars in relation to environment and diet. *J. Hum. Evol.* **119**, 42–63 (2018).
99. Lee-Thorp, J. A., van der Merwe, N. J. & Brain, C. K. Diet of *Australopithecus robustus* at Swartkrans from stable carbon isotopic analysis. *J. Hum. Evol.* **27**, 361–372 (1994).
100. Lee-Thorp, J., Thackeray, J. F. & van der Merwe, N. The hunters and the hunted revisited. *J. Hum. Evol.* **39**, 565–576 (2000).
101. Steininger, C. M. The Dietary Behaviour of Early Pleistocene Bovid from Cooper's Cave and Swartkrans, South Africa. PhD thesis, Univ. of the Witwatersrand (2011).
102. Adams, J. W. Stable carbon isotope analysis of fauna from the Gondolin GD 2 fossil assemblage, South Africa. *Ann. Ditsong Natl. Mus. Nat. Hist.* **2**, 1–5 (2012).
103. Reed, K. E. Early hominid evolution and ecological change through the African Plio-Pleistocene. *J. Hum. Evol.* **32**, 289–322 (1997).
104. de Ruiter, D. J., Sponheimer, M. & Lee-Thorp, J. A. Indications of habitat association of *Australopithecus robustus* in the Bloubaan Valley, South Africa. *J. Hum. Evol.* **55**, 1015–1030 (2008).
106. Kuman, K. & Clarke, R. J. Stratigraphy, artefact industries and hominid associations for Sterkfontein, member 5. *J. Hum. Evol.* **38**, 827–847 (2000).
107. Fashing, P. J., Nguyen, N., Venkataraman, V. V. & Kerby, J. T. Gelada feeding ecology in an intact ecosystem at Guassa, Ethiopia: variability over time and implications for theropit and hominin dietary evolution. *Am. J. Phys. Anthropol.* **155**, 1–16 (2014).
108. d'Huart, J.-P. in *Pigs, Peccaries, and Hippos: Status Survey and Conservation Action Plan* (ed. Oliver, W. L. R.) 84–92 (IUCN, Gland, 1993).
109. Quinn, R. L. et al. Pedogenic carbonate stable isotopic evidence for wooded habitat preference of early Pleistocene tool makers in the Turkana Basin. *J. Hum. Evol.* **65**, 65–78 (2013).
110. Robinson, J. R., Rowan, J., Campisano, C. J., Wynn, J. G. & Reed, K. E. Late Pliocene environmental change during the transition from *Australopithecus* to *Homo*. *Nat. Ecol. Evol.* **1**, 0159 (2017).
111. Signor, P. W. III & Lipps, J. H. in *Geological Implications of Impacts of Large Asteroids and Comets on the Earth* (eds Silver, L. T. & Schultz, P. H.) 291–296 (The Geological Society of America, Boulder, 1982).
112. White, T. D. in *Paleoclimate and Evolution, with Emphasis on Human Origins* (eds Vrba, E. S. et al.) 369–384 (Yale Univ. Press, New Haven, 1995).
113. Codron, D., Brink, J. S., Rossouw, L. & Clauss, M. The evolution of ecological specialization in southern African ungulates: competition- or physical environmental turnover? *Oikos* **117**, 344–353 (2008).
114. Wood, B. & Strait, D. Patterns of resource use in early *Homo* and *Paranthropus*. *J. Hum. Evol.* **46**, 119–162 (2004).
115. Moggi-Cecchi, J., Menter, C., Boccone, S. & Keyser, A. Early hominin dental remains from the Plio-Pleistocene site of Drimolen, South Africa. *J. Hum. Evol.* **58**, 374–405 (2010).
116. Klein, R. G., Avery, G., Cruz-Urbe, K. & Steele, T. E. The mammalian fauna associated with an archaic hominin skullcap and later Acheulean artifacts at Elandsfontein, Western Cape Province, South Africa. *J. Hum. Evol.* **52**, 164–186 (2007).
117. Brink, J. S. et al. First hominine remains from a ~1.0 million year old bone bed at Cornelia-Uitsoek, Free State Province, South Africa. *J. Hum. Evol.* **63**, 527–535 (2012).
118. Asfaw, B. et al. Remains of *Homo erectus* from Bouri, Middle Awash, Ethiopia. *Nature* **416**, 317–320 (2002).
119. Abbate, E. et al. A one-million-year-old *Homo* cranium from the Danakil (Afar) Depression of Eritrea. *Nature* **393**, 458–460 (1998).
120. Bahr, A. et al. Deciphering bottom current velocity and paleoclimate signals from contourite deposits in the Gulf of Cádiz during the last 140 kyr: an inorganic geochemical approach. *Geochim. Geophys. Geosci.* **15**, 3145–3160 (2014).
121. Adegbe, A. T., Schneider, R. R., Röhl, U. & Wefer, G. Glacial millennial-scale fluctuations in central African precipitation recorded in terrigenous sediment supply and freshwater signals offshore Cameroon. *Palaeogeogr. Palaeoclimatol. Palaeoecol.* **197**, 323–333 (2003).
122. Dickson, A. J., Leng, M. J., Maslin, M. A. & Röhl, U. Oceanic, atmospheric and ice-sheet forcing of South East Atlantic Ocean productivity and South African monsoon intensity during MIS-12 to 10. *Quat. Sci. Rev.* **29**, 3936–3947 (2010).
123. Revel, M. et al. 20,000 years of Nile River dynamics and environmental changes in the Nile catchment area as inferred from Nile upper continental slope sediments. *Quat. Sci. Rev.* **130**, 200–221 (2015).
124. Ziegler, M. et al. Development of Middle Stone Age innovation linked to rapid climate change. *Nat. Commun.* **4**, 1905 (2013).
125. Rohling, E. J. et al. Sea-level and deep-sea-temperature variability over the past 5.3 million years. *Nature* **508**, 477–482 (2014).
126. IAEA. *Isotope Hydrology Information System, The ISOHIS Database* <http://www.iaea.org/water> (2006).
127. Risi, C., Bony, S. & Vimeux, F. Influence of convective processes on the isotopic composition ( $\delta^{18}\text{O}$  and  $\delta\text{D}$ ) of precipitation and water vapor in the tropics: 2. physical interpretation of the amount effect. *J. Geophys. Res.* **113**, D19306 (2008).
128. Stock, W. D., Chuba, D. K. & Verboom, G. A. Distribution of South African C<sub>3</sub> and C<sub>4</sub> species of Cyperaceae in relation to climate and phylogeny. *Austral Ecol.* **29**, 313–319 (2004).
129. Dupont, L. M. & Kuhlmann, H. Glacial-interglacial vegetation change in the Zambezi catchment. *Quat. Sci. Rev.* **155**, 127–135 (2017).
130. Schrag, D. P. et al. The oxygen isotope composition of seawater during the Last Glacial Maximum. *Quat. Sci. Rev.* **21**, 331–342 (2002).
131. Sachse, D. et al. Molecular paleohydrology: interpreting the hydrogen-isotopic composition of lipid biomarkers from photosynthesizing organisms. *Annu. Rev. Earth Planet. Sci.* **40**, 221–249 (2012).
132. Collins, J. A. et al. Estimating the hydrogen isotopic composition of past precipitation using leaf-waxes from western Africa. *Quat. Sci. Rev.* **65**, 88–101 (2013).
133. Schefuß, E., Schouten, S., Jansen, J. H. & Sinninghe Damsté, J. S. African vegetation controlled by tropical sea surface temperatures in the mid-Pleistocene period. *Nature* **422**, 418–421 (2003).
134. Grinsted, A., Moore, J. C. & Jevrejeva, S. Application of the cross wavelet transform and wavelet coherence to geophysical time series. *Nonlinear Process. Geophys.* **11**, 561–566 (2004).
135. Schulz, M. & Mudelsee, M. REDFIT: estimating red-noise spectra directly from unevenly spaced paleoclimatic time series. *Comput. Geosci.* **28**, 421–426 (2002).
136. Imbrie, J. et al. in *Milankovitch and Climate: Understanding the Response to Astronomical Forcing* (eds Berger, A. et al.) 269–305 (Springer, Dordrecht, 1984).

137. Dirks, P. H. et al. Geological setting and age of *Australopithecus sediba* from southern Africa. *Science* **328**, 205–208 (2010).
138. Pickering, R. et al. *Australopithecus sediba* at 1.977 Ma and implications for the origins of the genus *Homo*. *Science* **333**, 1421–1423 (2011).
139. Berger, L. R., de Ruiter, D. J., Steininger, C. M. & Hancox, J. Preliminary results of excavations at the newly investigated Coopers D deposit, Gauteng, South Africa. *S. Afr. J. Sci.* **99**, 276–278 (2003).
140. de Ruiter, D. J. et al. New *Australopithecus robustus* fossils and associated U-Pb dates from Cooper's Cave (Gauteng, South Africa). *J. Hum. Evol.* **56**, 497–513 (2009).
141. Keyser, A. W., Menter, C. G., Moggi-Cecchi, J., Rayne Pickering, T. & Berger, L. R. Drimolen: a new hominid-bearing site in Gauteng, South Africa. *S. Afr. J. Sci.* **96**, 193–197 (2000).
142. Adams, J. W., Rovinsky, D. S., Herries, A. I. R. & Menter, C. G. Macromammalian faunas, biochronology and palaeoecology of the early Pleistocene Main Quarry hominin-bearing deposits of the Drimolen Palaeocave System, South Africa. *PeerJ* **4**, e1941 (2016).
143. Thackeray, J. F., Kirschvink, J. L. & Raub, T. D. Palaeomagnetic analyses of calcified deposits from the Plio-Pleistocene hominid site of Kromdraai, South Africa: news & views. *S. Afr. J. Sci.* **98**, 537–540 (2002).
144. Herries, A. I. R., Curnoe, D. & Adams, J. W. A multi-disciplinary seriation of early *Homo* and *Paranthropus* bearing palaeocaves in southern Africa. *Quat. Int.* **202**, 14–28 (2009).
145. Herries, A. I. R. & Adams, J. W. Clarifying the context, dating and age range of the Gondolin hominins and *Paranthropus* in South Africa. *J. Hum. Evol.* **65**, 676–681 (2013).
146. Braga, J., Fourvel, J.-B., Lans, B., Bruxelles, L. & Thackeray, J. F. in *Kromdraai. A Birthplace of Paranthropus in the Cradle of Humankind* (eds Braga, J. & Thackeray, J. F.) 1–16 (SUN, Stellenbosch, 2016).
147. Herries, A. I., Adams, J. W., Kuykendall, K. L. & Shaw, J. Speleology and magnetobiostratigraphic chronology of the GD 2 locality of the Gondolin hominin-bearing paleocave deposits, North West Province, South Africa. *J. Hum. Evol.* **51**, 617–631 (2006).
148. Adams, J. W., Herries, A. I., Kuykendall, K. L. & Conroy, G. C. Taphonomy of a South African cave: geological and hydrological influences on the GD 1 fossil assemblage at Gondolin, a Plio-Pleistocene paleocave system in the Northwest Province, South Africa. *Quat. Sci. Rev.* **26**, 2526–2543 (2007).
149. Curnoe, D. K. A. Contribution to the Question of Early *Homo* in Southern Africa: Researches into Dating, Taxonomy and Phylogeny Reconstruction. PhD thesis, Australian National University (1999).
150. Herries, A. I. & Shaw, J. Palaeomagnetic analysis of the Sterkfontein palaeocave deposits: implications for the age of the hominin fossils and stone tool industries. *J. Hum. Evol.* **60**, 523–539 (2011).
151. Granger, D. E. et al. New cosmogenic burial ages for Sterkfontein Member 2 *Australopithecus* and Member 5 Oldowan. *Nature* **522**, 85–88 (2015).
152. Gibbon, R. J. et al. Cosmogenic nuclide burial dating of hominin-bearing Pleistocene cave deposits at Swartkrans, South Africa. *Quat. Geochronol.* **24**, 10–15 (2014).
153. Curnoe, D., Grün, R., Taylor, L. & Thackeray, F. Direct ESR dating of a Pliocene hominin from Swartkrans. *J. Hum. Evol.* **40**, 379–391 (2001).
154. Pickering, R., Kramers, J. D., Hancox, P. J., de Ruiter, D. J. & Woodhead, J. D. Contemporary flowstone development links early hominin bearing cave deposits in South Africa. *Earth Planet. Sci. Lett.* **306**, 23–32 (2011).
155. Balter, V. et al. U–Pb dating of fossil enamel from the Swartkrans Pleistocene hominid site, South Africa. *Earth Planet. Sci. Lett.* **267**, 236–246 (2008).
156. Vrba, E. S. Some evidence of chronology and palaeoecology of Sterkfontein, Swartkrans and Kromdraai from the fossil Bovidae. *Nature* **254**, 301–304 (1975).
157. Vrba, E. S. in *L'environnement des hominidés au Plio-Pléistocène* (eds Beden, M. et al.) 345–369 (Masson, 1985).
158. Churcher, C. S. & Watson, V. in *Swartkrans: A Cave's Chronicle of Early Man* (ed. Brain, C. K.) 137–150 (Transvaal Museum, Pretoria, 1993).
159. Blackwell, B. A. Problems associated with reworked teeth in electron spin resonance (ESR) dating. *Quat. Sci. Rev.* **13**, 651–660 (1994).
160. Steininger, C. Local ecological profile for *Paranthropus robustus* in South Africa using stable carbon isotopes from associated bovid teeth. *Quat. Int.* **279–280**, 466 (2012).

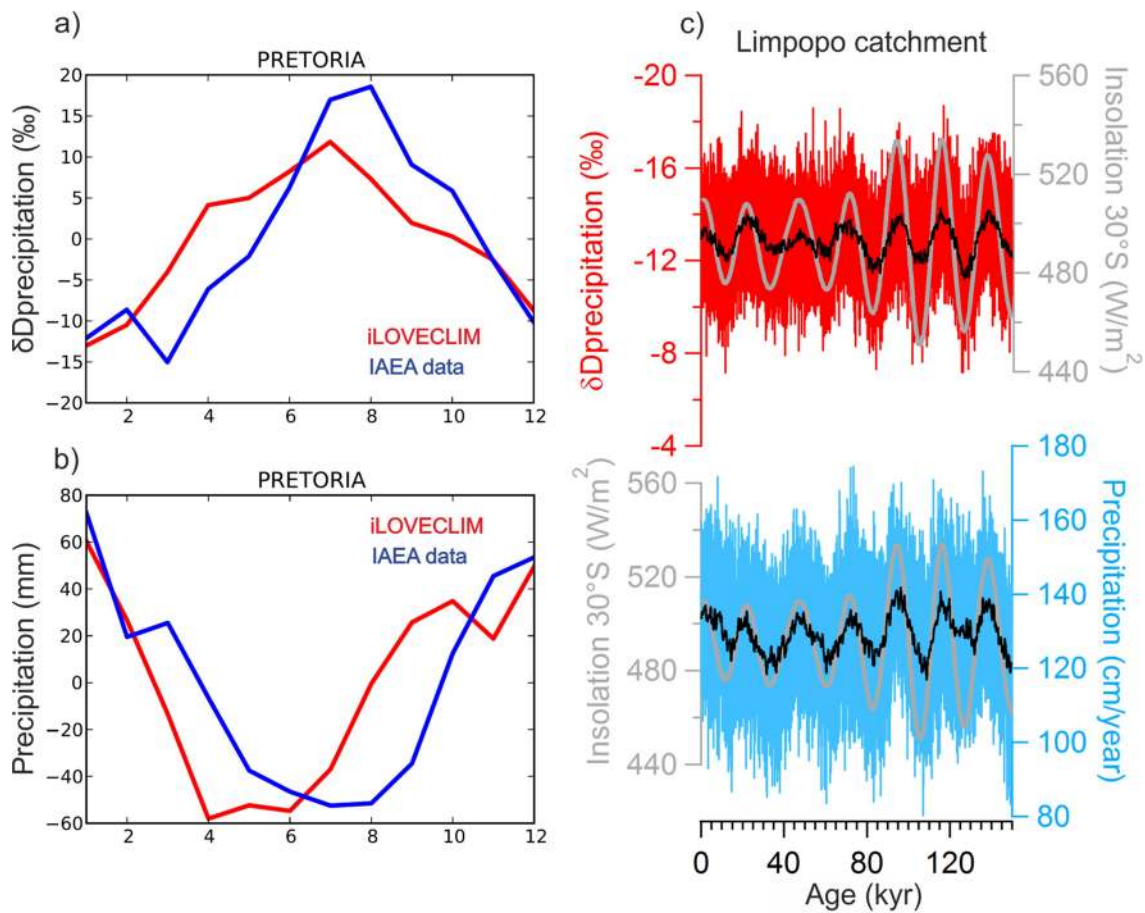




### Extended Data Fig. 1 | $\ln(\text{Fe}/\text{Ca})$ as a proxy for Limpopo runoff.

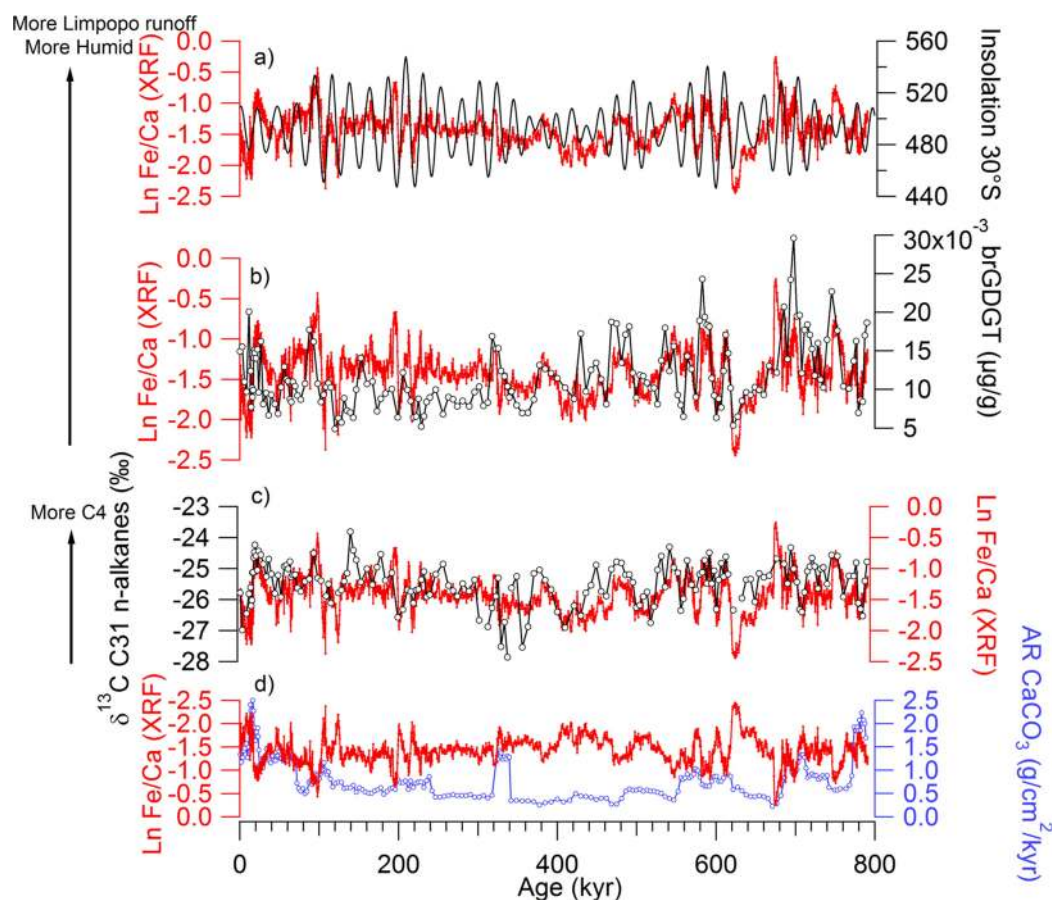
Calcium and iron both have complex and multiple origins in marine sediments. Iron can be related to redox variations, detrital and fluvial input, among others, and calcium can be related to the biogenic fraction (foraminifera or nannofossils) and detrital input. To properly interpret the  $\ln(\text{Fe}/\text{Ca})$  ratio at our study location, we applied principal components analysis<sup>120</sup>. **a**, PC1 describes 66% of the total variance for the entire site MD96-2048. The negative loadings for PC1 are calcium and strontium, and all other elements (aluminium, silicon, potassium, titanium, iron and zirconium) have positive loadings. Calcium and strontium are associated with biogenic carbonate and are mainly related to presence of foraminifera. Element matrix correlation shows a strong positive linear correlation ( $R > 0.70$ ) between iron and typically detrital elements, such as aluminium, silicon, titanium and potassium. Calcium shows negative correlation with iron ( $R = -0.5$ ). **b**,  $\ln(\text{Fe}/\text{Ca})$  shows a strong correlation with PC1 ( $R = 0.94$ ) and a strong relationship with Limpopo runoff

proxies (Extended Data Fig. 3). Iron and titanium elements are related to terrigenous and siliciclastic components (heavy minerals and oxides) and the variation in carbonate content (calcium) is mainly due to dilution by terrigenous sediment.  $\ln(\text{Fe}/\text{Ca})$  is therefore a proxy of Limpopo runoff, consistent with previous studies in riverine basins throughout the African continent<sup>10,121–124</sup>. To confirm a weak influence of sea-level changes on the Fe/Ca record, we compared our  $\ln(\text{Fe}/\text{Ca})$  record with a previous reconstruction of the deep-water  $\delta^{18}\text{O}$  component for relative sea level<sup>125</sup>, (**b**, bottom). Both records are plotted against the LR04 chronology. Visual inspection and statistical testing do not support a dominant effect of sea-level changes on the  $\ln(\text{Fe}/\text{Ca})$  record ( $R = 0.05$ ). PC3, which describes 11% of the total variance for the entire site MD96-2048, is closely related to sea-level changes. The negative loadings for PC3 are mainly strontium and, to a lesser degree, potassium and titanium, and the main positive loadings are zirconium and, to a lesser degree, silicon.



**Extended Data Fig. 2 | Control on the  $\delta D$  composition of precipitation in the Limpopo catchment.** **a, b,** Seasonal  $\delta D$  composition of precipitation (**a**) and amount of precipitation at Pretoria station<sup>126</sup> (**b**), in comparison to the results of the iLOVECLIM model at the corresponding latitude and longitude<sup>48,49</sup>. All data are centred on their annual average. Depleted  $\delta D$  values are indicative of increasing amounts of rainfall<sup>127</sup>. **c,** Results of the transient simulation with the isotope-enabled numerical climate model iLOVECLIM for the  $\delta D$  composition of precipitation and precipitation in

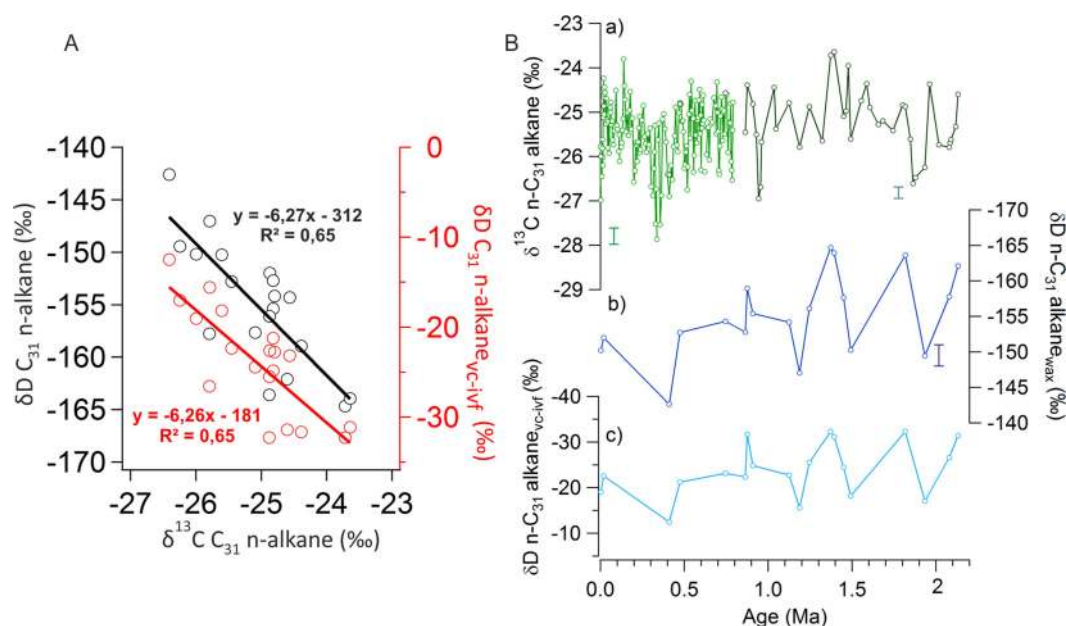
the Limpopo catchment (about  $-27.5^\circ \text{S}$  to  $-22^\circ \text{S}$  and  $30^\circ \text{E}$  to  $36^\circ \text{E}$ ), for the past 150 kyr (Methods)<sup>51</sup>. Black curves show the results after filtering with a low-pass filter. The  $\delta D$  composition of precipitation and precipitation amount in the Limpopo catchment are negatively correlated ( $R = -0.63$ ,  $P \ll 0.001$ ) for the past 150 kyr. Maxima of precipitation are phased with maxima in austral summer insolation at  $30^\circ \text{S}$  and lead to more-depleted  $\delta D_{\text{precipitation}}$  (amount effect).



**Extended Data Fig. 3 | Relationship between Limpopo runoff, local Southern Hemisphere insolation and the  $C_{31}$   $n$ -alkane  $\delta^{13}C$  record for the past 800 kyr.** **a**, Comparison between the  $\ln(Fe/Ca)$  XRF signal and austral summer local insolation at  $30^\circ S$ <sup>31</sup>. **b**, Comparison between the  $\ln(Fe/Ca)$  XRF signal and the brGDGT concentration in the sediment<sup>15</sup>. brGDGTs are commonly found in soil and can be attributed to Limpopo River runoff<sup>15</sup>. **c**, Comparison between the  $\ln(Fe/Ca)$  XRF signal and the  $C_{31}$   $n$ -alkane  $\delta^{13}C$  record<sup>16</sup>. An increased amount of Limpopo River discharge is associated with more  $C_4$  plant input and an increase in austral summer insolation at  $30^\circ S$ . **d**, Comparison between inverted  $\ln(Fe/Ca)$  XRF signal and the accumulation rate (AR) of  $CaCO_3$  as a measure of biogenic carbonate. The  $\ln(Fe/Ca)$  XRF record is not primarily controlled by dilution due to biological productivity ( $R=0.1$ ). A previous study of the past 0.8 Myr of core MD96-2048 interpreted shifts towards more-depleted  $\delta^{13}C_{wax}$  as potentially reflecting more-humid conditions<sup>16</sup>. However, the anti-correlation between  $\delta^{13}C_{wax}$  and  $\delta D_{wax}$  values (Extended Data Fig. 4)

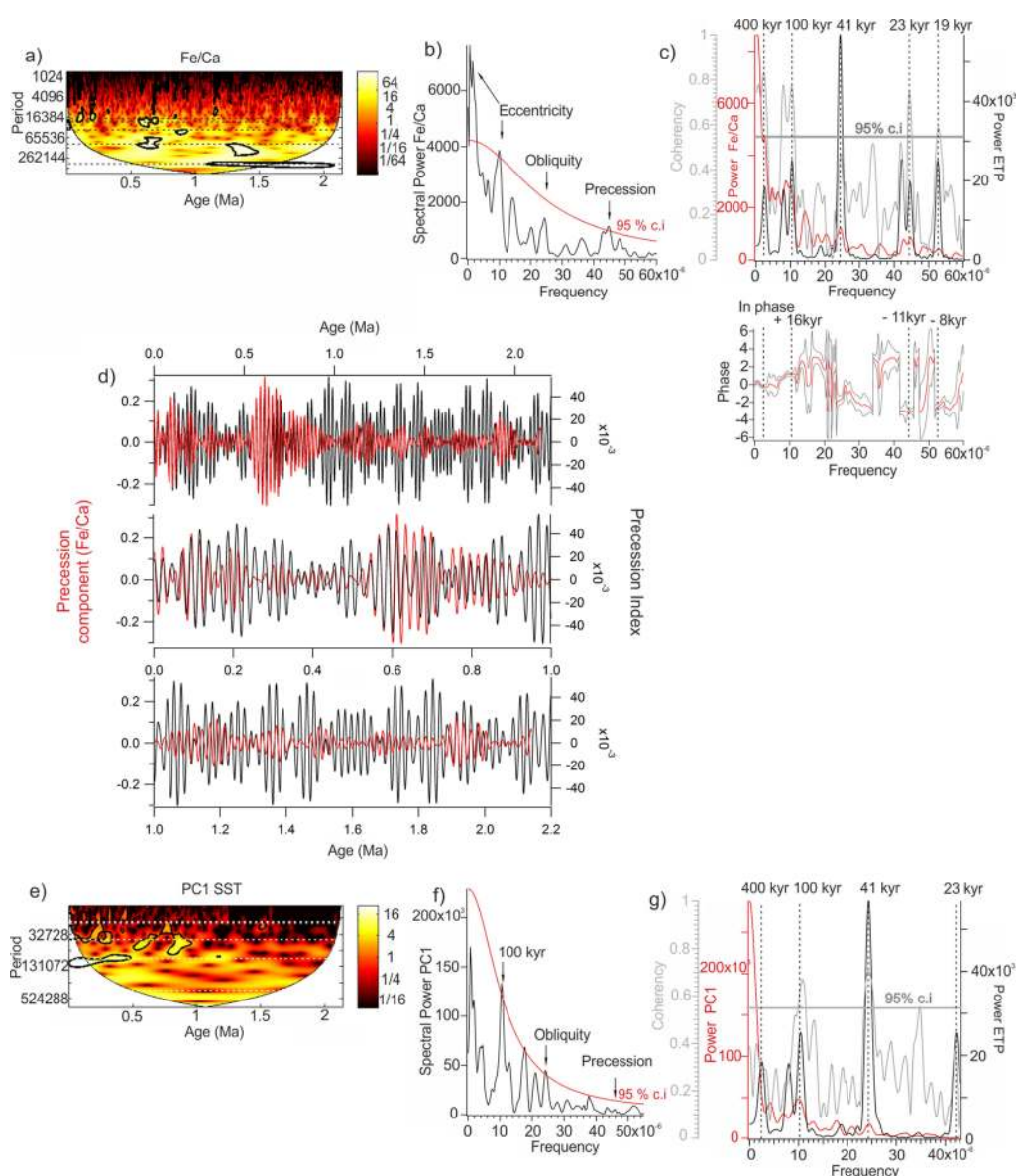
in our study indicates that enriched  $\delta^{13}C_{wax}$  values are associated with more-humid conditions. Because  $C_4$  plants in the Limpopo catchment are dominant in the interior (Fig. 1), we propose that more-enriched  $\delta^{13}C_{wax}$  values indicate a higher relative contribution from sources located farther upstream (more  $C_4$  plants) during times of high runoff, compared to only downstream sources (more  $C_3$  plants) during times of low discharge. In addition, humid conditions would have favoured the extension of sedge-rich vegetation (Cyperaceae, of which 20–60% are  $C_4$  plants in this region<sup>128</sup>) in riverine swamps and floodplains along the river course, explaining the detected increase in Cyperaceae pollen at times of increased fluvial discharge (Fig. 2). Studies of sediments from the adjacent Zambezi catchment similarly suggest the extension of swampy sedge-rich vegetation—including  $C_4$ -Cyperaceae—when river discharge was high, and infer that more  $C_4$  plant waxes are exported to the ocean when the flooding of floodplains occurs during rainfall maxima<sup>10,129</sup>.





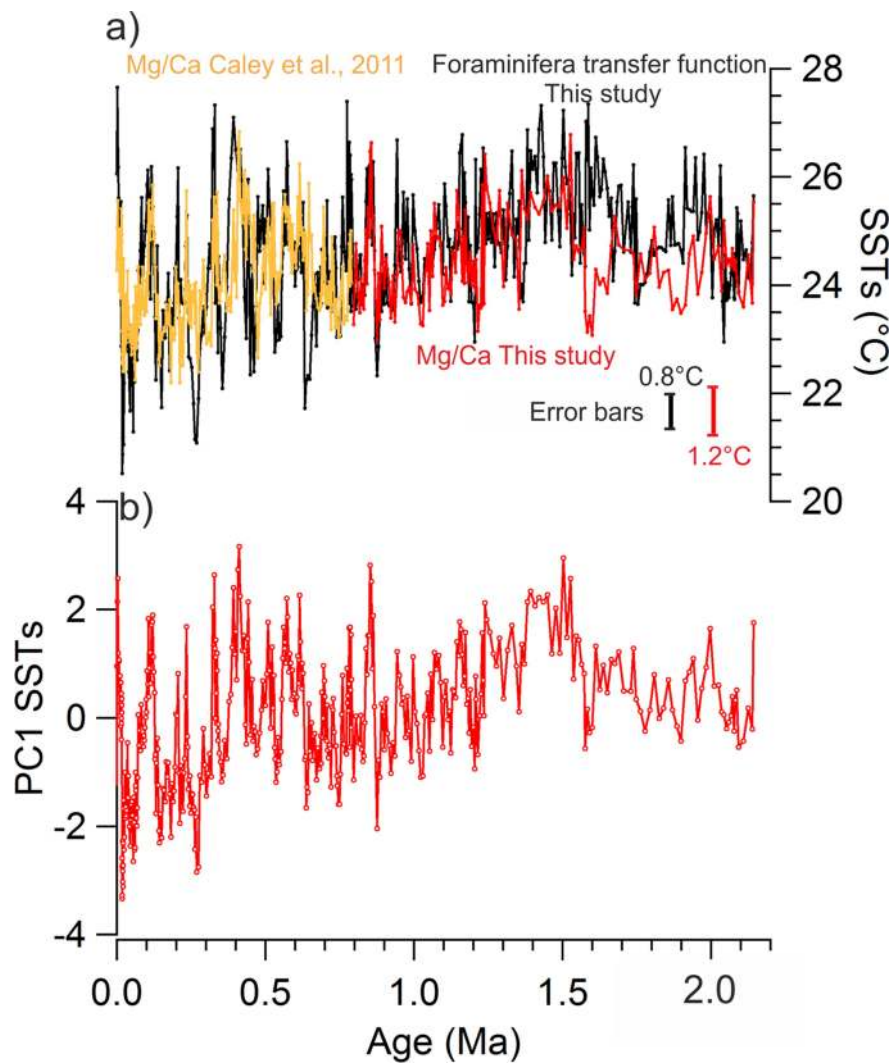
**Extended Data Fig. 4 | Relation between the  $\delta^{13}\text{C}_{\text{C}_{31}}$  n-alkanes record and the  $\delta\text{D}_{\text{C}_{31}}$  n-alkanes record. a**, Correlation between the record of  $\delta^{13}\text{C}_{\text{C}_{31}}$  n-alkanes and the record of  $\delta\text{D}_{\text{C}_{31}}$  n-alkanes, with or without vegetation and ice-volume correction (vc-ivf) over the past 2.14 Myr ( $n = 19$  samples). An anti-correlation exists between the  $\delta^{13}\text{C}$  and the  $\delta\text{D}$  signals of the  $\text{C}_{31}$  n-alkanes. The  $\text{C}_{31}$  n-alkane is used because it is the most abundant homologue in the samples. **b**, Raw  $\delta^{13}\text{C}_{\text{wax}}$ ,  $\delta\text{D}_{\text{wax}}$  data and  $\delta\text{D}_{\text{wax}}$  adjusted for ice-volume and vegetation changes from core MD96-2048. Mean analytical uncertainties are indicated. Top,  $\delta^{13}\text{C}_{\text{wax}}$  of the  $\text{C}_{31}$  homologue (data from a previous study<sup>16</sup> in light green, and data from this study in dark green). Middle,  $\delta\text{D}_{\text{wax}}$  of the  $\text{C}_{31}$  homologue. Bottom,  $\delta\text{D}_{\text{wax}}$  of the  $\text{C}_{31}$  homologue adjusted for ice-volume changes (ivf) using a seawater  $\delta^{18}\text{O}$  curve<sup>125</sup> and converting to  $\delta\text{D}$  assuming an increase of 7.2‰ at the Last Glacial Maximum. We use 7.2‰ because measurements of sediment pore water  $\delta^{18}\text{O}$  and  $\delta\text{D}$  suggest that the glacial ocean  $\delta\text{D}$  increase has a mean value of 7.2‰<sup>130</sup>. We also adjusted the

$\delta\text{D}_{\text{wax}}$  record for vegetation changes (vc) using published fractionation factors ( $-123\text{‰} \pm 31\text{‰}$  for  $\text{C}_3$  trees,  $-139\text{‰} \pm 27\text{‰}$  for  $\text{C}_4$  grasses<sup>131</sup>) and the  $\delta^{13}\text{C}_{\text{wax}}$  signal following a previously published procedure<sup>132</sup>. End-member  $\delta^{13}\text{C}_{\text{wax}}$  values used for  $\text{C}_3$  and  $\text{C}_4$  vegetation were  $-36\text{‰}$  and  $-21.5\text{‰}$ , respectively<sup>133</sup>. The error ranges for the vegetation fractionation factors are very large<sup>131</sup>. They derive from the compilation of a global dataset from individual plants, which is not comparable to an ecosystem fractionation in a specific catchment (such in the Limpopo) that will fractionate with a much smaller uncertainty. However, as we do not know the exact fractionation factor in the Limpopo catchment and regard the uncertainties from the global compilation as unrealistic for a specific ecosystem we refrained from propagating this uncertainty into the vegetation corrections. The vegetation and ice-volume-adjusted  $\delta\text{D}_{\text{wax}}$  record is very similar to the unadjusted record, highlighting the fact that the adjustments have a minor effect.



**Extended Data Fig. 5 | Statistical analyses for the  $\ln(\text{Fe}/\text{Ca})$  XRF record and PC1 SST record.** **a**, Spectral power for  $\ln(\text{Fe}/\text{Ca})$  by wavelet analysis realized with a previously published MatLab package<sup>134</sup>. The thick contour designates the 5% significance level against red noise. Dashed black lines indicate the variability at the precession, obliquity and eccentricity periods. **b**, Spectral analysis of  $\ln(\text{Fe}/\text{Ca})$  with REDFIT<sup>135</sup>. The red line shows the false-alarm level at the 95% confidence interval. Spectral peaks exceeding the false-alarm level can be considered significant<sup>135</sup>. **c**, Blackman–Tukey cross correlation between  $\ln(\text{Fe}/\text{Ca})$  XRF and eccentricity–tilt–precession (ETP) realized with the Analyseries software<sup>37</sup> for the past 2.14 Myr. ETP is constructed by normalizing and stacking eccentricity, tilt (obliquity) and negative precession to evaluate coherence and phase (timing) relative to orbital extremes<sup>136</sup>. The red curve shows the spectral power for  $\ln(\text{Fe}/\text{Ca})$  record. The black curve shows the spectral power for ETP. The coherence, which varies between 0 and 1, is represented by the grey curve and gives the interval within which the spectrum is significant. In our case, the non-zero coherence is higher than 0.55 and is significant at the 95% confidence interval (grey line). There

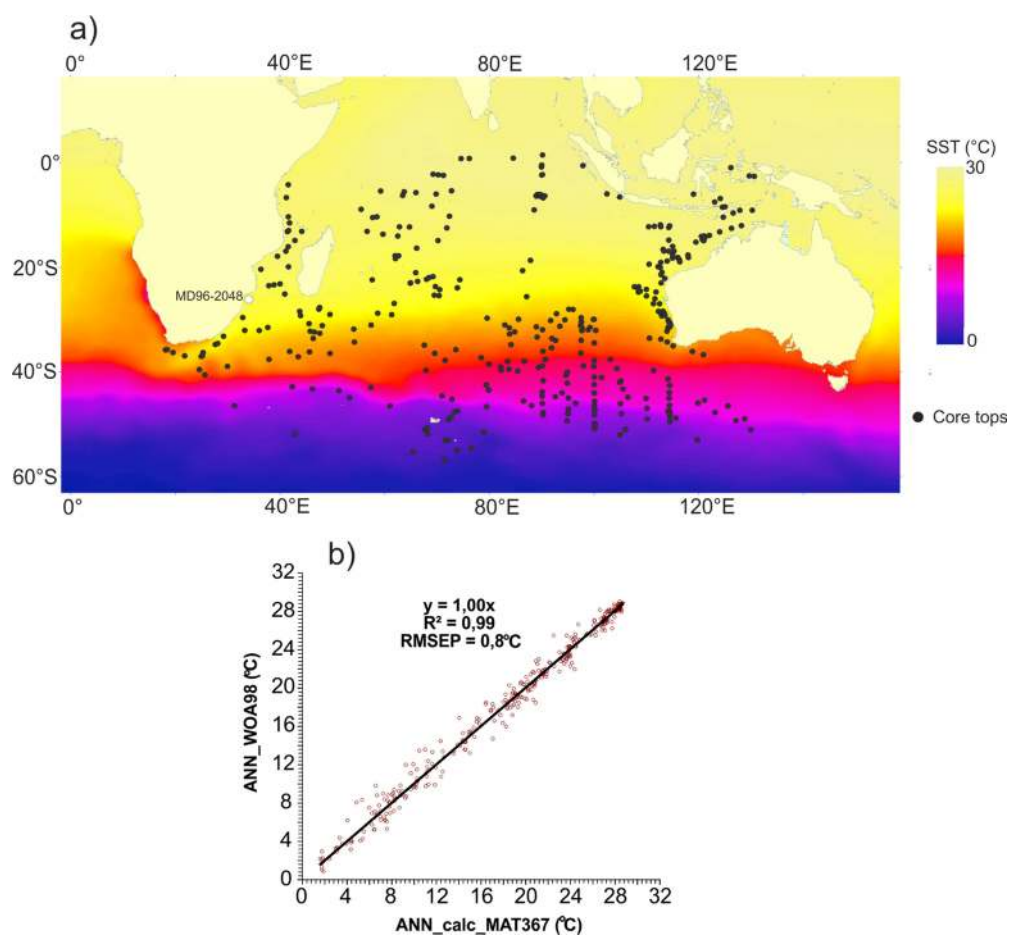
are significant spectral peaks for eccentricity and precession but not for obliquity. The  $\ln(\text{Fe}/\text{Ca})$  XRF record and ETP are in phase at the 400-kyr period, the eccentricity leads by 16 kyr the  $\ln(\text{Fe}/\text{Ca})$  record at the 100-kyr period and the  $\ln(\text{Fe}/\text{Ca})$  record is in anti-phase with negative precession (in-phase with positive precession) at the 19- and 23-kyr periods. The three statistical analyses are consistent and indicate significant variability at the 400-, 100-, 23- and 19-kyr periods and insignificant variability at the 41-kyr period. **d**, Comparison between the precessional component of the  $\ln(\text{Fe}/\text{Ca})$  record (Gaussian filter frequency  $1/23,000$ ; bandwidth:  $5 \times 10^{-6}$ ) obtained with the Analyseries software<sup>37</sup> and the precession index. Maxima of the  $\ln(\text{Fe}/\text{Ca})$  precession component are in phase with precession index maxima. The precession cycles in the  $\ln(\text{Fe}/\text{Ca})$  record appear particularly strong between about 0.9 and 0.6 Ma. **e–g**, The same statistical analyses as in **a–c**, respectively, but for the PC1 SST record. In **e**, dashed white lines indicate the variability at the precession, obliquity and eccentricity periods. The three statistical analyses indicate significant variability at the 100- and 41-kyr periods but not significant power for the 400-kyr and 23-kyr (precession) periods.



**Extended Data Fig. 6 | Reconstruction using SST proxies for core MD96-2048 for the past 2.14 Myr. a,** Reconstruction of SST using two different methods: Mg/Ca reconstruction based on previous<sup>15</sup> and new data (Mg/Ca ratios were converted into temperature values by applying a previously established equation<sup>40</sup>) and foraminifera transfer function

reconstruction using the modern analogue technique. Error bars represent the error on the calibrations<sup>40</sup> (Extended Data Fig. 7). **b,** Empirical orthogonal function analysis<sup>47</sup> of the two SST records for the past 2.14 Myr. PC1 contains 74% of the total variance for the past 2.14 Myr. Correlation between SST proxies and PC1 for the past 2.14 Myr is  $R = 0.71$ .





**Extended Data Fig. 7 | Foraminifera transfer function used for core MD96-2048.** **a.** Location of the modern database, composed of 367 core tops from the south Indian Ocean<sup>45</sup> with present-day SST from the World Ocean Atlas (WOA) 2009<sup>29</sup>. **b.** Test for the modern database<sup>45</sup> yielding

to a precision of 0.8°C for the annual SST reconstructions. Modern hydrological parameters were obtained from the WOA (1998) database using a previously developed tool (<http://www.geo.uni-bremen.de/geomod/Sonst/Staff/csn/woasample.html>).

Extended Data Table 1 | Fossil finds, their location and associated ages

Site/area	Taxon	Stratigraphic unit	Methods	References	Estimated age of fossils
Malapa	<i>Australopithecus sediba</i>		Biochronology	Dirks et al. (137)	From 1.95 Ma to 1.78 Ma
			U-Pb dating of flowstones: basal flowstone 1 at $2.026 \pm 0.021$ Ma; capping flowstone 2 at $2.048 \pm 0.140$ Ma	Pickering et al. (138)	From 2.188 Ma to 1.908 Ma
			Paleomagnetism : reversed polarity of flowstone 2, normal polarity of fossiliferous sediments	Pickering et al. (138)	Older than 1.95 Ma
			Synthesis of flowstone dating and paleomagnetism, $1.977 \pm 0.002$ Ma	Pickering et al. (138)	<b>From 1.979 to 1.975 Ma</b>
Cooper's D	<i>Paranthropus robustus</i>		Biochronology	Berger et al. (139)	From 1.9 Ma to 1.6 Ma
			U-Pb dating of flowstones: basal flowstone CDD1 at $1.526 \pm 0.088$ Ma; younger flowstone CDD3, intercalated within fossiliferous sequence, at ca. 1.4 Ma (unprecise dating from 1.617 Ma to 1.413 Ma)	de Ruiter et al. (140)	<b>From 1.615 Ma to ca. 1.4 Ma (upper facies A and C) and younger than 1.4 Ma (lower facies A and C)</b>
Drimolen	<i>P. robustus</i>	Main Quarry Site	Biochronology	Keyser et al. (141)	From 2.0 Ma to 1.5 Ma
			Biochronology	Adams et al. (142)	<b>From 2.3 Ma to 1.6 Ma</b>
Kromdraai B	<i>P. robustus</i>		Paleomagnetism of flowstone above Mb. 3, reverse polarity, older than normal Olduvai event (between 1.95 Ma and 1.78 Ma)	Thackeray et al. (143)	Older than 1.95 Ma
			Alternative interpretation of paleomagnetic data from Thackeray et al. (2002)	Herries et al. (144); Herries & Adams (145)	From 1.78 Ma to 1.65 Ma
			Biochronology (including hominins) and paleomagnetism	Braga et al. (146)	Older than 2.18 Ma
Gondolin	<i>P. robustus</i>	GD2*	Biochronology and paleomagnetism (Olduvai normal polarity event of fossiliferous sediments)	Herries et al. (147)	<b>Slightly older than 1.78 Ma</b>
	<i>P. robustus</i>	GD1*	Biochronology and paleomagnetism (end of Olduvai normal polarity event in basal flowstone)	Adams et al. (148)	<b>Slightly younger than 1.78 Ma</b>
Sterkfontein	<i>P. robustus</i>	Mb. 5B "Oldowan infill"	Biochronology and lithic typology	Kuman & Clarke (106)	From 2.0 Ma to 1.7 Ma
			ESR on bovid teeth (seven dates): $1.328 \pm 0.087$ Ma; $1.315 \pm 0.295$ Ma; $1.185 \pm 0.96$ Ma; $1.265 \pm 0.125$ Ma; $1.620 \pm 0.626$ Ma; $0.965 \pm 0.147$ Ma; $1.24 \pm 0.28$ Ma; weighed mean = $1.32 \pm 0.08$ Ma	Curnoe (149) reinterpreted in Herries & Shaw (150)	From 1.40 Ma to 1.24 Ma
		Mb. 5B "Oldowan infill"	Synthesis of ESR, U-Pb dating, paleomagnetism	Herries & Shaws (150)	From ca. 1.4 Ma to 1.2 Ma
			ESR on teeth from $0.965 \pm 0.147$ Ma to $1.328 \pm 0.087$ Ma ; weighted mean LU-ESR (excluding one tooth with large internal errors) = $1.223 \pm 0.155$ Ma	Curnoe (149) reinterpreted in Herries et al. (144)	From 1.415 Ma to 1.241 Ma (maximal); 1.112 Ma to 0.818 Ma (minimal); from 1.378 Ma to 1.223 (weighed mean)
		Mb. 5B "Oldowan infill"	Cosmogenic burial ( $^{26}\text{Al}/^{10}\text{Be}$ ) dating of a quartz manuport $2.18 \pm 0.21$ Ma	Granger et al. (151)	From 2.39 Ma to 1.97 Ma
		Mb. 5B "Oldowan infill"	Synthesis of paleomagnetism, U-Pb dating, and ESR	Herries & Adams (145)	From 1.8 Ma to 1.5 Ma
		Mb. 5B "Oldowan infill"	Synthesis of biochronology and ESR	Herries et al. (144)	From 1.38 Ma to 1.07 Ma
Swartkrans	<i>P. robustus</i>	Mb. 1	Cosmogenic burial ( $^{26}\text{Al}/^{10}\text{Be}$ ) dating on quartz $2.19 \pm 0.08$ Ma	Gibbon et al. (152)	From 2.27 Ma to 2.11 Ma
		Mb. 1	Cosmogenic burial ( $^{26}\text{Al}/^{10}\text{Be}$ ) dating on quartz $1.80 \pm 0.09$ Ma	Gibbon et al. (152)	From 1.89 Ma to 1.71 Ma
		Mb. 1 Hanging Remnant	Synthesis of U-Pb dating and ESR	Herries & Adams (145)	From 2.0 Ma to 1.8 Ma
		Mb. 1 Hanging Remnant	ESR $2.02 \pm 0.36$ Ma; $2.07 \pm 0.37$ Ma; $1.68 \pm 0.28$ Ma; weighed mean = 1.96 Ma-1.70 Ma	Curnoe et al. (153) reinterpreted in Herries & Adams (145)	From 1.96 Ma to 1.70 Ma
		Mb. 1 Hanging Remnant	ESR LU $1.39 \pm 0.18$ Ma	Herries et al. (144)	From 1.57 Ma to 1.21 Ma
		Mb. 1 Hanging Remnant	ESR LU $1.92 \pm 0.34$ Ma	Herries et al. (144)	From 2.26 Ma to 1.58 Ma
		Mb. 1 Hanging Remnant	ESR LU $1.21 \pm 0.22$ Ma	Herries et al. (144)	From 1.43 Ma to 0.99 Ma
		Mb. 1 Lower Bank	U-Pb dating	Pickering et al. (154)	From 2.3 to 1.6 Ma
		Mb. 1	U-Pb dating on tooth $1.83 \pm 1.38$ Ma	Balter et al. (155)	From 3.21 to 0.45 Ma
		Mb. 1	Biochronology	Vrba (156, 157); Churcher & Watson (158)	ca. 1.7 Ma
		Mb. 1	U-Pb dating of basal flowstone $2.249 \pm 0.077$ Ma; top flowstone $1.706 \pm 0.069$ Ma ; closer to 2.0 Ma-1.8 Ma	Pickering et al. (154)	<b>Maximal range from 2.326 Ma to 1.637 Ma; minimal range from 2.172 Ma to 1.775 Ma</b>
Swartkrans	<i>P. robustus</i>	Mb. 2	U-Pb dating on tooth $1.36 \pm 0.29$ Ma	Balter et al. (155)	<b>From 1.65 Ma to 1.07 Ma</b>
		Mb. 2	Biochronology	Vrba (156, 157); Churcher & Watson (158)	ca. 1.5 Ma
		Mb. 2	Relative position to Mb. 1 dated by U-Pb	Pickering et al. (154)	Younger than ca. 1.7 Ma
Swartkrans	<i>P. robustus</i>	Mb. 3	Synthesis of U-Pb and ESR dating	Herries & Adams (145)	From 1.3 Ma to 0.6 Ma
		Mb. 3	Cosmogenic burial on quartz $0.96 \pm 0.09$ Ma	Gibbon et al. (152)	<b>From 1.05 Ma to 0.87 Ma</b>
		Mb. 3	ESR $0.65 \pm 0.15$ Ma	Cited in Herries and Adams (145)	From 0.8 Ma to 0.5 Ma
		Mb. 3	ESR $1.25 \pm 0.09$ Ma	Cited in Herries and Adams (145)	From 1.34 Ma to 1.16 Ma
		Mb. 3	U-Pb dating on tooth $0.83 \pm 0.21$ Ma	Balter et al. (155)	<b>From 1.04 Ma to 0.62 Ma</b>
		Mb. 3	Biochronology	Vrba (156, 157); Churcher & Watson (158)	ca. 1.0 Ma
		Mb. 3	ESR LU on two bovid teeth (four dates): $0.71 \pm 0.90$ Ma and $0.80 \pm 0.15$ Ma; $0.65 \pm 0.15$ Ma and $0.70 \pm 0.11$ Ma; mean = $0.72 \pm 0.13$ Ma	Blackwell (159)	From 0.85 Ma to 0.59 Ma
		Mb. 3	Synthesis of biochronology and U-Pb	Herries et al. (144)	<b>From 1.04 Ma to 0.62 Ma</b>

Data in this table were taken from refs<sup>106,137–160</sup>. We consider the ages in bold as the best estimate. The different dating methods did not yield any agreement regarding the age of Kromdraai B and Sterkfontein member 5 'Oldowan Infill'. Therefore, no estimate is highlighted in bold and the stratigraphic ranges are not shown in Fig. 3. We favour U–Pb dates and cosmogenic burial of quartz dates rather than biochronology or electron spin resonance, although dates produced using the latter two methods are generally not inconsistent with those produced using the other methods<sup>145</sup>. \**P. robustus* fossils were not found at Gondolin GD 1 and GD 2 but nearby ex situ. Given the close age between Gondolin GD 1 and GD 2 deposits and the limited extent of outcrops, it has been suggested<sup>145</sup> that the ex situ hominin specimens from Gondolin are dated to around 1.78 Ma.

**Extended Data Table 2 |  $\delta^{13}\text{C}$  enamel of hominin and contemporaneous herbivores and associated statistical parameters for different sites in the Limpopo catchment**

Group	$\delta^{13}\text{C}$ (‰)			mode(s) (2 ‰ interval)	SD	min	max range		References
	n	mean	median						
Cooper' D herbivores	45	-5,0	-4,7	int. 1: -12 to -10 ‰ ; int. 2: -2 to 0 ‰	3,9	-11,5	2,5	14,0	Steininger (101)
Gondolin GD2 herbivores	21	-2,9	1,0	int. 1: -10 to -8 ‰ ; int. 2: 0 to 2 ‰	5,3	-11,1	3,5	14,6	Adams (102)
Swartkrans Mb. 1 herbivores	56	-4,8	-3,8	int. 1: -10 to -8 ‰ ; int. 2: -4 to 0 ‰	4,2	-12,4	2,2	14,6	Lee-Thorp et al. (99); Sponheimer et al. (83); Steininger (160)
Swartkrans Mb. 1 <i>Paranthropus</i>	18	-7,2	-6,9	int.: -8 to -6 ‰	1,2	-9,6	-4,9	4,7	Lee-Thorp et al. (99); Sponheimer et al. (84, 83)
Swartkrans Mb. 1 <i>Homo</i>	3	-8,2	-8,2	int.: -10 to -8 ‰	0,9	-9,2	-7,1	2,1	Lee-Thorp et al. (100)
Swartkrans Mb. 2 herbivores	53	-4,8	-3,8	int. 1: -12 to -10 ‰ ; int. 2: -4 to -2 ‰	4,4	-12,9	2,2	15,1	Lee-Thorp et al. (99, 100); Steininger (160)
Swartkrans Mb. 2 <i>Paranthropus</i>	2	-9,1	-9,1			-10,0	-8,1	1,9	Lee-Thorp et al. (99)
Swartkrans Mb. 3 herbivores	12	-3,8	-2,2	int.: -4 to 0 ‰	3,3	-11,6	-0,5	11,1	Steininger (160)
Swartkrans Mb. 3 <i>Paranthropus</i>	1	-7,9	-7,9			-7,9	-7,9		Lee-Thorp et al. (99)